A UNIFIED JET MODEL OF X-RAY FLASHES, X-RAY–RICH GAMMA-RAY BURSTS, AND GAMMA-RAY BURSTS. I. POWER-LAW–SHAPED UNIVERSAL AND TOP-HAT–SHAPED VARIABLE OPENING ANGLE JET MODELS

D. Q. LAMB, T. Q. DONAGHY, AND C. GRAZIANI

Department of Astronomy and Astrophysics, University of Chicago, 5640 South Ellis Avenue, Chicago, IL 60637;
d-lamb@uchicago.edu, quinn@oddjob.uchicago.edu, carlo@oddjob.uchicago.edu

ABSTRACT

HETE-2 has provided strong evidence that the properties of X-ray flashes (XRFs), X-ray–rich gamma-ray bursts (GRBs), and GRBs form a continuum, and therefore that these three kinds of bursts are the same phenomenon. A key feature found by *HETE-2* is that the density of bursts is roughly constant per logarithmic interval in burst fluence S_E and observed spectral peak energy E_{peak}^{obs}, and in isotropic-equivalent energy E_{iso} and spectral peak energy E_{peak} in the rest frame of the burst. In this paper, we explore a unified jet model of all three kinds of bursts, using population synthesis simulations of the bursts and detailed modeling of the instruments that detect them. We show that both a variable jet opening angle model in which the emissivity is a constant independent of the angle relative to the jet axis and a universal jet model in which the emissivity is a power-law function of the angle relative to the jet axis can explain the observed properties of GRBs reasonably well. However, if one tries to account for the properties of XRFs, X-ray–rich GRBs, and GRBs in a unified picture, the extra degree of freedom available in the variable jet opening angle model enables it to explain the observations reasonably well while the power-law universal jet model cannot. The variable jet opening angle model of XRFs, X-ray–rich GRBs, and GRBs implies that the energy E_γ radiated in gamma rays is $\sim$100 times less than has been thought. The model also implies that most GRBs have very small jet opening angles ($\sim$half a degree). This suggests that magnetic fields may play an important role in GRB jets. It also implies that there are $\sim 10^4$–10^5 more bursts with very small jet opening angles for every burst that is observable. If this is the case, the rate of GRBs could be comparable to the rate of Type Ic core-collapse supernovae. These results show that XRFs may provide unique information about the structure of GRB jets, the rate of GRBs, and the nature of Type Ic supernovae.

Subject headings: gamma rays: bursts — ISM: jets and outflows — shock waves — supernovae: general

Online material: color figure

1. INTRODUCTION

One-third of all *HETE-2*–localized bursts are ''X-ray–rich'' gamma-ray bursts (GRBs), and an additional one-third are X-ray flashes (XRFs)[1] (Sakamoto et al. 2004b). The latter have received increasing attention in the past several years (Heise et al. 2000; Kippen et al. 2003), but their nature remains largely unknown.

XRFs have t_{90} durations between 10 and 200 s, and their sky distribution is consistent with isotropy (Heise et al. 2000). In these respects, XRFs are similar to GRBs. A joint analysis of WFC/BATSE spectral data showed that the low-energy and high-energy photon indices of XRFs are -1 and about -2.5, respectively, which are similar to those of GRBs, but that the XRFs have spectral peak energies E_{peak}^{obs} that are much lower than those of GRBs (Kippen et al. 2003). The only difference between XRFs and GRBs therefore appears to be that XRFs have lower E_{peak}^{obs} values. It has therefore been suggested that XRFs might represent an extension of the GRB population to bursts with low peak energies, and that the distinction between XRFs and GRBs is driven by instrumental considerations rather than by any sharp intrinsic difference between the two kinds of bursts (Kippen et al. 2003; Barraud et al. 2003; Sakamoto et al. 2004b).

A number of theoretical models have been proposed to explain XRFs. Yamazaki et al. (2002, 2003) have proposed that

XRFs are the result of a highly collimated GRB jet viewed well off the axis of the jet. In this model, the low values of E_{peak} and E_{iso} (and therefore of E_{peak}^{obs} and S_E) seen in XRFs are the result of relativistic beaming. However, it is not clear that such a model can produce roughly equal numbers of XRFs, X-ray–rich GRBs, and GRBs and still satisfy the observed relation between E_{iso} and E_{peak} (Amati et al. 2002; Lamb et al. 2004d).

According to Mészáros et al. (2002) and Zhang et al. (2004b), X-ray (20–100 keV) photons are produced effectively by the hot cocoon surrounding the GRB jet as it breaks out, and could produce XRF-like events if viewed well off the axis of the jet. However, it is not clear that such a model would produce roughly equal numbers of XRFs, X-ray–rich GRBs, and GRBs, or the nonthermal spectra exhibited by XRFs.

The ''dirty fireball'' model of XRFs posits that baryonic material is entrained in the GRB jet, resulting in a bulk Lorentz factor $\Gamma \ll 300$ (Dermer et al. 1999; Huang et al. 2002; Dermer & Mitman 2004). At the opposite extreme, GRB jets in which the bulk Lorentz factor $\Gamma \gg 300$ and the contrast between the bulk Lorentz factors of the colliding relativistic shells are small can also produce XRF-like events (Mochkovitch et al. 2004).

In this paper, we explore a unified jet picture of XRFs, X-ray–rich GRBs, and GRBs, motivated by *HETE-2* observations of the three kinds of bursts. We consider two different phenomenological jet models: a variable jet opening angle model in which the emissivity is a constant independent of the angle relative to the jet axis, and a universal jet model in which the emissivity is a power-law function of the angle relative to the

---

[1] We define ''X-ray–rich'' GRBs and XRFs as those events for which $\log\left[S_X(2-30 \text{ keV})/S_\gamma(30-400 \text{ keV})\right] > -0.5$ and 0.0, respectively.

jet axis. We show that the variable jet opening angle model can account for the observed properties of all three kinds of bursts. In contrast, we find that although the power-law universal jet model can account reasonably well for the observed properties of GRBs, it cannot easily be extended to account for the observed properties of XRFs and X-ray–rich GRBs.

This paper is organized as follows. In § 2 we summarize the results of *HETE-2* observations of XRFs, X-ray–rich GRBs, and GRBs. In § 3 we define the variable jet opening angle model and the power-law universal jet model. In § 4 we describe our simulations, detailing how we model the bursts themselves, propagate the bursts to the Earth, and model the instruments that detect them. In § 5 we compare our results with observations, and in § 6 we discuss their implications. In § 7 we present our conclusions. Preliminary results were reported in Lamb et al. (2004a, 2004b, 2004c).

2. OBSERVATIONS OF X-RAY FLASHES AND GAMMA-RAY BURSTS

2.1. *HETE-2 Results*

Clarifying the nature of XRFs and their connection to GRBs could provide a breakthrough in our understanding of the prompt emission of GRBs and of the structure of XRF and GRB jets. Analyzing 45 bursts seen by the FREGATE (Atteia et al. 2003) and/or the WXM (Kawai et al. 2003) instruments on *HETE-2* (Ricker et al. 2003), Sakamoto et al. (2004b) find that XRFs, X-ray–rich GRBs, and GRBs form a continuum in the $[S_E(2-400 \text{ keV}), E_{\text{peak}}^{\text{obs}}]$-plane (see Fig. 1), where $S_E(2-400 \text{ keV})$ is the fluence of the burst in the 2–400 keV energy band and $E_{\text{peak}}^{\text{obs}}$ is the energy of the observed peak of the burst spectrum in νF_ν.

Furthermore, Lamb et al. (2004d) have placed nine *HETE-2* GRBs with known redshifts and two XRFs with known redshifts or strong redshift constraints in the $(E_{\text{iso}}, E_{\text{peak}})$-plane (see Fig. 2). Here E_{iso} is the isotropic-equivalent burst energy and E_{peak} is the energy of the peak in the burst νF_ν spectrum, measured in the source frame. We define E_{iso} to be the energy emitted in the source-frame passband from 1 to 10000 keV. This definition is a suitable bolometric quantity for both GRBs and XRFs and is the same definition of E_{iso} used by Amati et al. (2002). The *HETE-2* results confirm the correlation between E_{iso} and E_{peak} found by Lloyd-Ronning et al. (2000) for BATSE bursts and the relation between these two quantities found by Amati et al. (2002) for *BeppoSAX* bursts with known redshifts, and the results extend the relation down in E_{iso} by a factor of ~300. The fact that XRF 020903 (Sakamoto et al. 2004a), the softest burst localized by *HETE-2* to date, and XRF 030723 (Prigozhin et al. 2003) lie squarely on this relation (Lamb et al. 2004d) is evidence that the relation between E_{iso} and E_{peak} extends down in E_{iso} by a factor of ~300 and applies to XRFs and X-ray–rich GRBs, as well as to GRBs. However, additional redshift determinations are clearly needed for XRFs with 1 keV < E_{peak} < 30 keV in order to confirm this.

Lamb et al. (2004d) show that, using *HETE-2* and *BeppoSAX* GRBs with known redshifts and XRFs with known redshifts or strong redshift constraints, there is also a relation between the isotropic-equivalent burst luminosity L_{iso} and E_{peak} that extends over 5 decades in L_{iso} and (as must then be the case) between E_{iso} and L_{iso} that extends over 5 decades in both (see Fig. 2). Yonutoku et al. (2004) have confirmed the relation between L_{iso} and E_{peak} for GRBs, while Liang et al. (2004) have shown that this relation holds within GRBs.

Thus, the *HETE-2* results show that the properties of XRFs, X-ray–rich GRBs, and GRBs form a continuum in the $[S_E(2-$
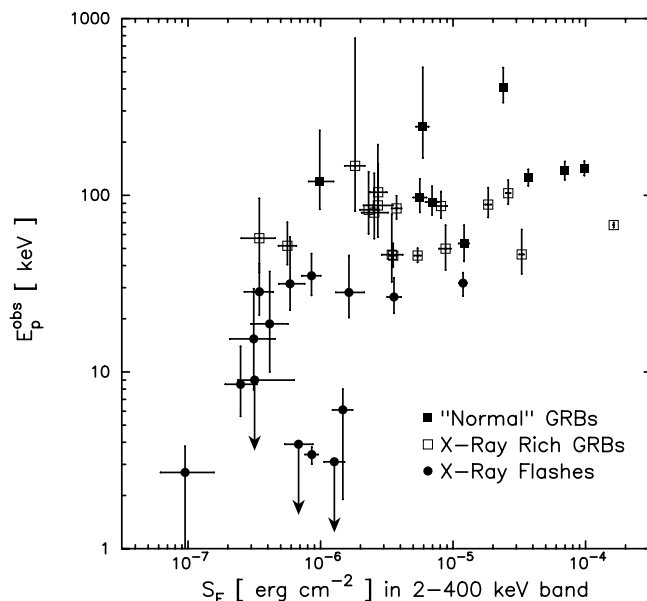

Fig. 1.—Distribution of *HETE-2* bursts in the $[S(2-400 \text{ keV}), E_{\text{peak}}^{\text{obs}}]$-plane, showing XRFs (*filled circles*), X-ray–rich GRBs (*open boxes*), and GRBs (*filled boxes*). This figure shows that XRFs and X-ray–rich GRBs comprise about two-thirds of the bursts observed by *HETE-2* and that the properties of the three kinds of bursts form a continuum. All error bars are 90% confidence level. From Sakamoto et al. (2004b).

400 keV), $E_{\text{peak}}^{\text{obs}}$]-plane and that the relation between E_{iso} and E_{peak} extends to XRFs and X-ray–rich GRBs. A key feature of the distributions of bursts in these two planes is that the density of bursts is roughly constant along these relations, implying roughly equal numbers of bursts per logarithmic interval in S_E, $E_{\text{peak}}^{\text{obs}}$, E_{iso}, and E_{peak}. These results, when combined with the earlier results described above, strongly suggest that all three kinds of bursts are the same phenomenon. It is this possibility that motivates us to seek a unified jet model of XRFs, X-ray–rich GRBs, and GRBs.

2.2. *Evidence That Most GRBs Have a "Standard" Energy*

Frail et al. (2001) and Panaitescu & Kumar (2001) (see also Bloom et al. 2003) find that most GRBs have a "standard" energy. That is, most GRBs have the same radiated energy, $E_\gamma = 1.3 \times 10^{51}$ ergs, to within a factor of ~2–3, if their isotropic equivalent energy is corrected for the jet opening angle θ_{jet} inferred from the jet break time. This is illustrated in Figure 3, which shows the distribution of total radiated energies in gamma rays (E_γ) for 24 GRBs, after taking into account the jet opening angle inferred from the jet break time (Bloom et al. 2003).

Pursuing this picture further, we show in Figure 4 the distribution of E_{iso}, L_{iso}, and E_{peak} as a function of $2\pi/\Omega_{\text{jet}}$ for the *HETE-2* and *BeppoSAX* GRBs with known redshifts. Figure 4 shows that all three quantities are strongly correlated with Ω_{jet}. The correlation between E_{iso} and Ω_{jet} is implied by the fact that most GRBs have a standard energy (Frail et al. 2001; Panaitescu & Kumar 2001). The correlation between L_{iso} and Ω_{jet} is implied by the fact that most GRBs have a standard energy and by the correlation between E_{iso} and L_{iso} (Lamb et al. 2004d). The correlation between E_{peak} and Ω_{jet} is implied by the fact that most GRBs have a standard energy, by the correlation between E_{iso} and E_{peak} found by Lloyd-Ronning et al. (2000) for BATSE bursts without redshifts, and by the tight relation between E_{iso} and E_{peak} found by Amati et al. (2002) for *BeppoSAX* bursts with
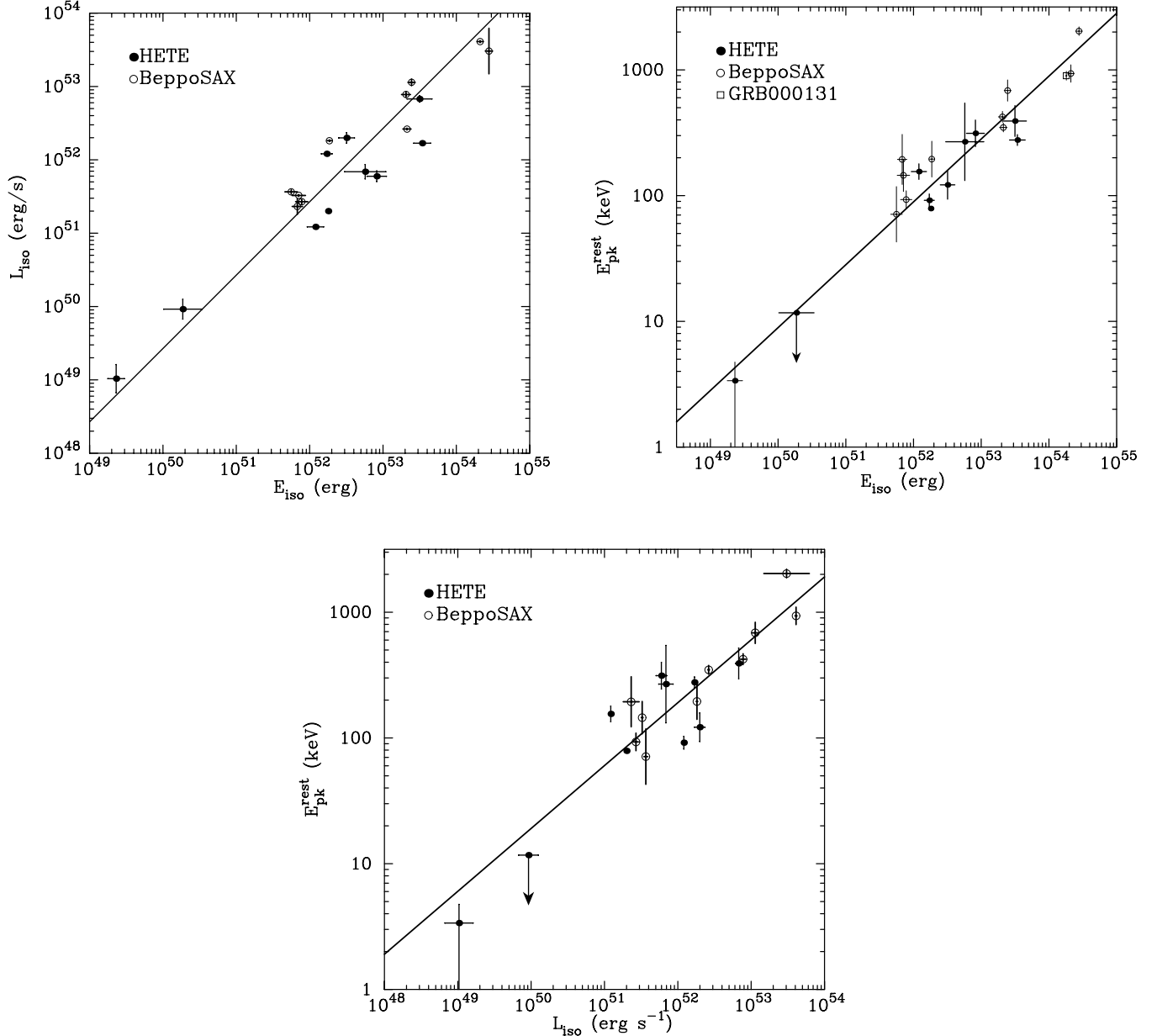
Fig. 2.—*Top left*: Distribution of *HETE-2* and *BeppoSAX* bursts in the (E_{iso}, L_{iso})-plane, where E_{iso} and L_{iso} are the isotropic-equivalent GRB energy and luminosity in the source frame. *Top right*: Distribution of *HETE-2* and *BeppoSAX* bursts in the (E_{iso}, E_{peak})-plane, where E_{peak} is the energy of the peak of the burst νF_ν spectrum in the source frame. The *HETE-2* bursts confirm the relation between E_{iso} and E_{peak} found by Amati et al. (2002) and extend it by a factor of $\sim$300 in E_{iso}. *Bottom*: Distribution of *HETE-2* and *BeppoSAX* bursts in the (L_{iso}, E_{peak})-plane. The distribution of *HETE-2* and *BeppoSAX* bursts in the three planes demonstrates that there is a linear relation between log E_{iso} and log L_{iso} that extends over at least five decades in both quantities, and that there are linear relations between both log E_{iso} and log L_{iso} and log E_{peak} that extend over at least 2.5 decades in E_{peak}. The bursts with the lowest and second-lowest values of E_{iso} and L_{iso} are XRFs 020903 and 030723. From Lamb et al. (2004d); *BeppoSAX* data are from Amati et al. (2002).

known redshifts. Figure 4 demonstrates these three correlations directly.

The strength of the correlations of all three quantities with Ω_{jet} lends additional support to a picture in which most GRBs have a standard energy and the observed ranges of $\sim$10^5 in E_{iso} and L_{iso} are due either to differences in the jet opening angle θ_{jet} or to differences in the viewing angle θ_{view} of the observer with respect to the axis of the jet. We pursue both of these possibilities below.

3. JET MODELS OF GAMMA-RAY BURSTS

Two phenomenological models of GRB jets have received widespread attention:

1. The universal jet model (Fig. 5a). In this model, all GRBs produce jets with the same structure (Rossi et al. 2002; Zhang & Mészáros 2002a; Mészáros et al. 2002; Perna et al. 2003; Zhang et al. 2004a, 2004b). The energy E_{iso} and luminosity L_{iso} are assumed to decrease as the viewing angle θ_{view} increases. The wide range of observed values of E_{iso} is then attributed to differences in the viewing angle θ_{view}. In order to recover the standard-energy result (Frail et al. 2001; Panaitescu & Kumar 2001; Bloom et al. 2003) over a wide range in viewing angles, $E_{iso}(\theta_{view}) \propto \theta_{view}^{-2}$ is required (Rossi et al. 2002; Zhang & Mészáros 2002a).

2. The variable jet opening angle model (Fig. 5b). In this model, GRB jets have a wide range of jet opening angles θ_{jet} (Frail et al. 2001). For $\theta_{view} < \theta_{jet}$, $E_{iso}(\theta_{view}) \approx$ constant, while
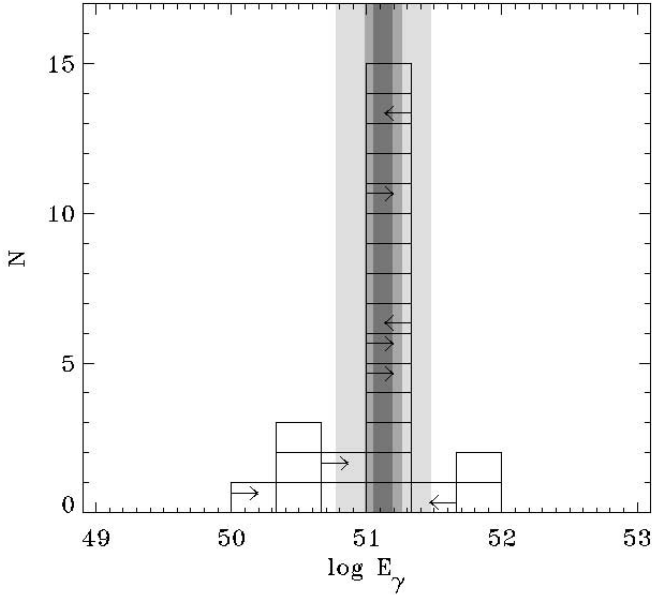
Fig. 3.—Distribution of the total energy E_γ radiated in gamma rays by GRBs, taking into account the jet opening angle inferred from the jet break time. From Bloom et al. (2003). [*See the electronic edition of the Journal for a color version of this figure.*]

for $\theta_{view} > \theta_{jet}$, $E_{iso}(\theta_{view}) = 0$. The wide range of observed values of E_{iso} is then attributed to differences in the jet opening angle θ_{jet}. This is the model that Frail et al. (2001) and Bloom et al. (2003) assume in deriving a standard energy for most bursts.

As described in the previous section, there is evidence that the relation between E_{iso} and E_{peak} extends over at least 5 decades in E_{iso} and appears to hold for XRFs and X-ray–rich GRBs, as well as for GRBs (Lamb et al. 2004d); most bursts appear to have a standard energy (Frail et al. 2001; Panaitescu & Kumar 2001; Bloom et al. 2003); and there are correlations among E_{iso}, L_{iso}, and E_{peak}, and between these quantities and Ω_{jet} (Frail et al. 2001; Bloom et al. 2003; Lamb et al. 2004d). Motivated by these results, we make three key assumptions in exploring a unified jet picture of all three kinds of bursts:

1. We assume that most XRFs, X-ray–rich GRBs, and GRBs have a standard energy E_γ with a modest scatter.

2. We assume that for most GRBs, E_{iso} and E_{peak} obey the relation (Lloyd-Ronning et al. 2000; Amati et al. 2002; Lamb et al. 2004d)

$$E_{peak} \propto (E_{iso})^{1/2} \qquad (1)$$

with a modest scatter, and that this relation holds for XRFs and X-ray–rich GRBs, as well as for GRBs.

3. We assume that the observed ranges of $\sim 10^5$ in E_{iso} and L_{iso} are due either to differences in the jet opening angle θ_{jet} (in the variable jet opening angle model) or to differences in the viewing angle θ_{view} of the observer with respect to the axis of the jet (in the universal jet model).

4. SIMULATIONS OF OBSERVED GAMMA-RAY BURSTS

4.1. *Overview of the Simulations*

We begin by giving an overview of our population synthesis simulations of observed GRBs before describing the simulations in mathematical detail. Our overall approach is to simulate the GRBs that are observed by different instruments by

(1) modeling the bursts in the source frame; (2) propagating the bursts from the source frame to us, using the cosmology that we have adopted; and (3) determining which bursts are observed and the properties of these bursts by modeling the instruments that observe them.

This logical sequence is evident in Figure 6, which shows a flowchart of the calculations involved in our simulations of bursts in the variable jet opening angle model. For each simulated burst we obtain a redshift z and a jet opening solid angle Ω_{jet} by drawing from specific distributions. In addition, we introduce three lognormal smearing functions to generate a timescale T, a jet energy E_γ, and a coefficient for the E_{iso}-E_{peak} relation (C). Using these five quantities, we calculate various rest-frame quantities (E_{iso}, L_{iso}, E_{peak}, etc.). Finally, we construct a Band spectrum for each burst and transform it into the observer frame, which allows us to calculate fluences and peak fluxes and to determine whether the burst would be detected by various experiments.

Astronomical observations usually impose strong observational selection effects on the population of objects being observed. Consequently, the most rigorous approach to comparing models to data, and finding the best-fit parameters for these models, is to specify the models being compared, independent of any observations. This avoids the pitfall of circularity, in which the posited models are already distorted by strong observational selection effects. In practice, this approach is difficult to carry out, particularly when our understanding of the phenomenon of interest is quite limited, as is currently the case for GRB jets.

We therefore adopt an intermediate approach in this paper. We use those properties of GRBs that we have reason to believe are unlikely to be strongly affected by observational selection effects as a guide in specifying the models that we consider. We then extend the predictions of these models to regimes in which the observational selection effects are strong by modeling these effects in detail. We are then able to compare the predictions of the models with observations in the regimes where we believe observational selection effects are unlikely to be important and in the regimes where we know that observational selection effects are important.

4.2. *GRB Rest-Frame Quantities*

4.2.1. *Variable Jet Opening Angle Model*

In this paper we investigate a variable jet opening angle model in which the emissivity is a constant independent of the angle relative to the jet axis and the distribution of jet opening angles is a power law. In a subsequent paper, we investigate variable jet opening angle models in which the emissivity is a constant independent of the angle relative to the jet axis and the distribution of jet opening angles is a Gaussian, and in which the emissivity is a Gaussian function of the angle relative to the jet axis and the distribution of jet opening angles is a power law (Donaghy et al. 2004a).

We assume that the emission from the jet is visible only when $\theta_{view} < \theta_{jet}$. In reality, emission from the jet may be seen when the observer is outside the opening angle of the jet, because of relativistic beaming effects. However, the angular width of the annulus within which the jet is visible (i.e., has a flux above some minimum observable flux) is small. If the opening angle of the jet is large (as is posited to be the case for XRFs in the variable jet opening angle model), the relative number of bursts that will be detectable because of relativistic beaming is therefore also small (T. Q. Donaghy 2005, in preparation). If the
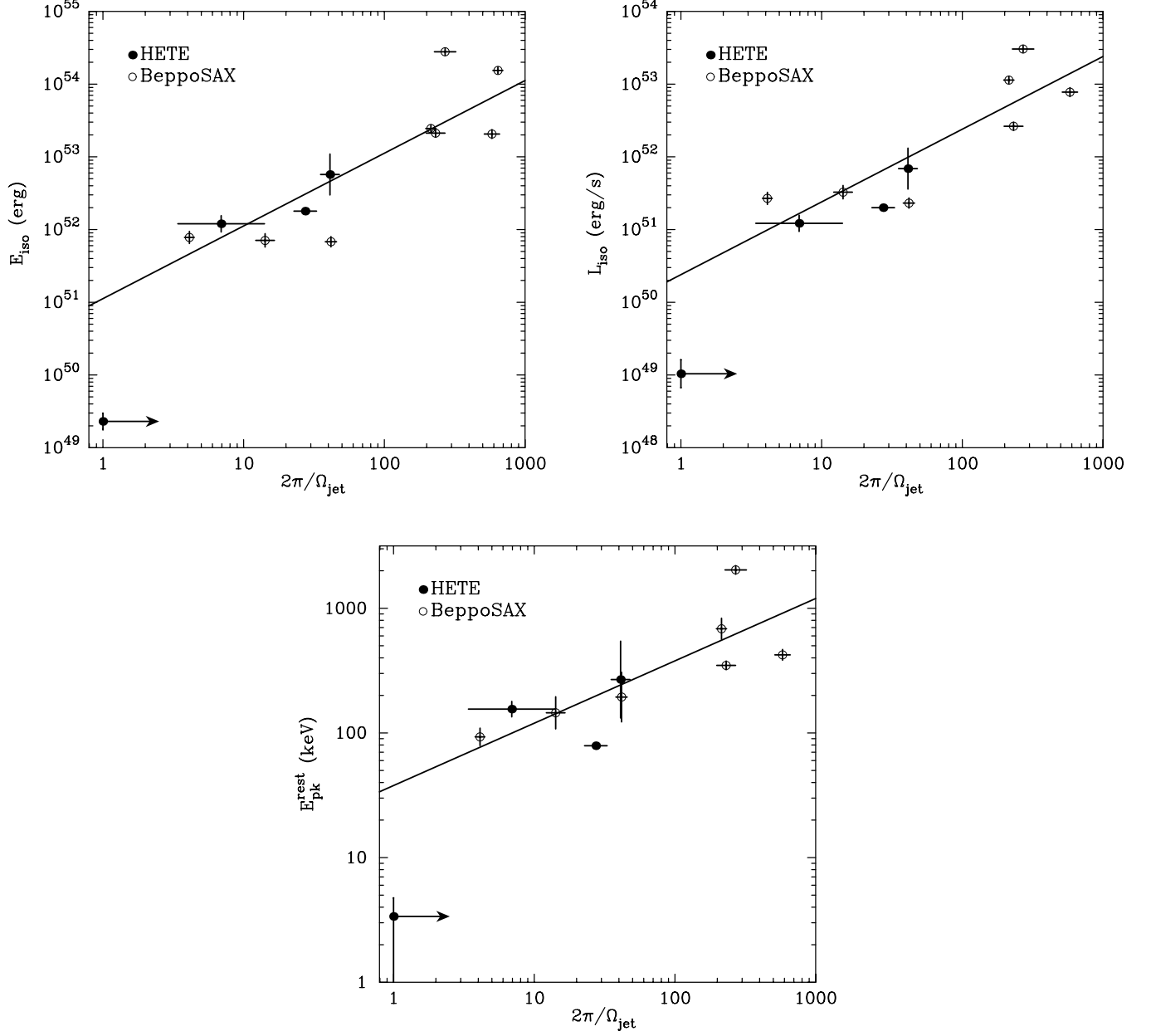
Fig. 4.—*Top left*: Distribution of *HETE-2* and *BeppoSAX* bursts in the $(2\pi/\Omega_{\rm jet}, E_{\rm iso})$-plane, where $E_{\rm iso}$ is the isotropic-equivalent burst energy in the source frame. In the variable jet opening angle model, $\Omega_{\rm jet}$ is the jet solid angle; in the power-law universal jet model it is the solid angle interior to the viewing angle $\theta_{\rm view}$. *Top right*: Distribution of *HETE-2* and *BeppoSAX* bursts in the $(2\pi/\Omega_{\rm jet}, L_{\rm iso})$-plane, where $L_{\rm iso}$ is the isotropic-equivalent burst luminosity in the source frame. *Bottom*: Distribution of *HETE-2* and *BeppoSAX* bursts in the $(2\pi/\Omega_{\rm jet}, E_{\rm peak})$-plane, where $E_{\rm peak}$ is the energy of the peak of the burst νF_ν spectrum in the source frame. The distribution of *HETE-2* and *BeppoSAX* bursts in these three planes demonstrates that there are linear relations between both $\log E_{\rm iso}$ and $\log L_{\rm iso}$ and $\log \Omega_{\rm jet}^{-1}$ that extend over at least 2.5 decades in $\log E_{\rm iso}$ and $\log L_{\rm iso}$, and a relation of slope 1/2 between $\log E_{\rm peak}$ and $\log \Omega_{\rm jet}^{-1}$ that extends over at least a decade in $E_{\rm peak}$. The event in the lower left corner is XRF 020903, which is shown as a lower limit in $2\pi/\Omega_{\rm jet}$. Data on $\Omega_{\rm jet}$ are from Bloom et al. (2003).
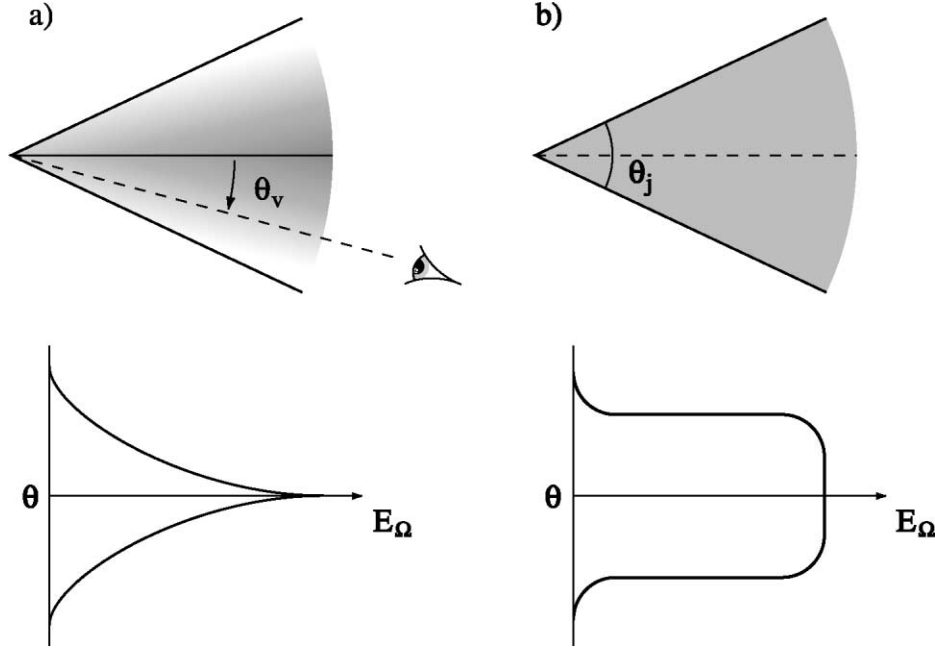
FIG. 5.—Schematic diagrams of the power-law universal and variable opening angle jet models of GRBs from Ramirez-Ruiz & Lloyd-Ronning (2002). In the power-law universal jet model, the isotropic-equivalent energy and luminosity are assumed to decrease as the viewing angle $\theta_{\rm view}$ as measured from the jet axis increases. In order to recover the standard-energy result (Frail et al. 2001), $E_{\rm iso}(\theta_{\rm view}) \sim \theta_{\rm view}^{-2}$ is required. In the variable jet opening angle model, GRBs produce jets with a large range of jet opening angles $\theta_{\rm jet}$. For $\theta_{\rm view} < \theta_{\rm jet}$, $E_{\rm iso}(\theta_{\rm view}) \approx$ constant, while for $\theta_{\rm view} > \theta_{\rm jet}$, $E_{\rm iso}(\theta_{\rm view}) = 0$. In this paper, we take $\theta_{\rm jet}$ to be the half-opening angle of the jet.

opening angle of the jet is small (as is posited to be the case for GRBs in the variable jet opening angle model), the bulk Γ in the jet may be large and the flux due to relativistic beaming that is seen by an observer outside the opening angle will then drop off precipitously. The relative number of bursts that will be detectable because of relativistic beaming is therefore again small (T. Q. Donaghy 2005, in preparation).

The distribution in jet opening solid angle $\Omega_{\rm jet}$ then generates our GRB luminosity function; here we are primarily interested in a power-law distribution. We define the fraction of the sky subtended by the GRB jet to be

$$f_{\rm jet} = \frac{\Omega_{\rm jet}}{2\pi} = 1 - \cos\theta_{\rm jet}. \quad (2)$$

We define the true distribution of opening angles to be

$$P_{\rm true}(\Omega_{\rm jet})d\Omega_{\rm jet} = {\rm const} \times (\Omega_{\rm jet})^{-\delta}d\Omega_{\rm jet} \quad (3)$$

over a range $(\Omega_{\rm jet}^{\rm min}, \Omega_{\rm jet}^{\rm max})$. We define the observed distribution of opening angles to be

$$P_{\rm obs}(\Omega_{\rm jet})d\Omega_{\rm jet} = {\rm const} \times (\Omega_{\rm jet})^{-\delta_{\rm sim}}d\Omega_{\rm jet} \propto f_{\rm jet}^{-\delta_{\rm sim}}. \quad (4)$$

Since we can observe only those bursts whose jets are oriented toward the Earth, the distribution of opening angles of observable bursts is related to the true distribution of opening angles by

$$P_{\rm obs}(\Omega_{\rm jet}) = f_{\rm jet} P_{\rm true}(\Omega_{\rm jet}) \propto (\Omega_{\rm jet})^{(1-\delta)}. \quad (5)$$

We thus simulate bursts using the power-law index $\delta_{\rm sim}$ from which the true power-law index can be found using the relation $\delta = 1 + \delta_{\rm sim}$.

The isotropic-equivalent emitted energy $E_{\rm iso}$ is then given by

$$E_{\rm iso} = \frac{E_\gamma}{f_{\rm jet}} = \frac{E_\gamma}{(\Omega_{\rm jet}/2\pi)}, \quad (6)$$

where E_γ is the total radiated energy of the burst. Using a full maximum likelihood approach, we reproduce the parameters of the lognormal distribution derived by Bloom et al. (2003), using their sample of GRBs with observed jet break times (see Fig. 7). We find no evidence for any correlation of E_γ with redshift (see again Fig. 7). We therefore draw values for E_γ randomly from the narrow lognormal distribution defined by

$$G(E_\gamma)d\log E_\gamma = \exp\left[\frac{-(\log E_\gamma - \log E_\gamma^0)^2}{2\sigma_E^2}\right]d\log E_\gamma, \quad (7)$$

where $\log E_\gamma^0$ (ergs) $= 51.070$ and $\log \sigma_E = 0.35$ (see also Table 1).

Our simulations thus use a value $E_\gamma^0 = 1.17 \times 10^{51}$ ergs, which is fully consistent with the value $E_\gamma^0 = 1.33 \times 10^{51}$ ergs found by Bloom et al. (2003). However, the Bloom et al. sample of GRBs contained no XRFs. The values of $E_{\rm iso}$ for XRFs 020903 (Sakamoto et al. 2004a) and 030723 (Lamb et al. 2004d) are ~ 100 times lower than the value of E_γ derived by Frail et al. (2001) and Bloom et al. (2003). Thus there is no value of the opening solid angle $\Omega_{\rm jet}$ that can accommodate these values of $E_{\rm iso}$. Since we are pursuing a unified jet model of XRFs, X-ray–rich GRBs, and GRBs, we must be able to accommodate values of $E_{\rm iso}$ that are ~ 100 times less than the value of E_γ derived by Frail et al. (2001) and Bloom et al. (2003).

We therefore introduce the ability to rescale $\log E_\gamma^0$, the central value of E_γ. This is equivalent to rescaling the range of $\Omega_{\rm jet}$, since only $E_{\rm iso}$ is observed. In doing so, we note that the derivation of E_γ is dependent on the coefficient in front of the relation between the jet break time and $\theta_{\rm jet}$, and that the value of this coefficient is uncertain by a factor of 4–5 (Rhoads 1999; Sari et al. 1999).

This rescaling of E_γ introduces an additional parameter $C_{\rm jet}$ into our model:

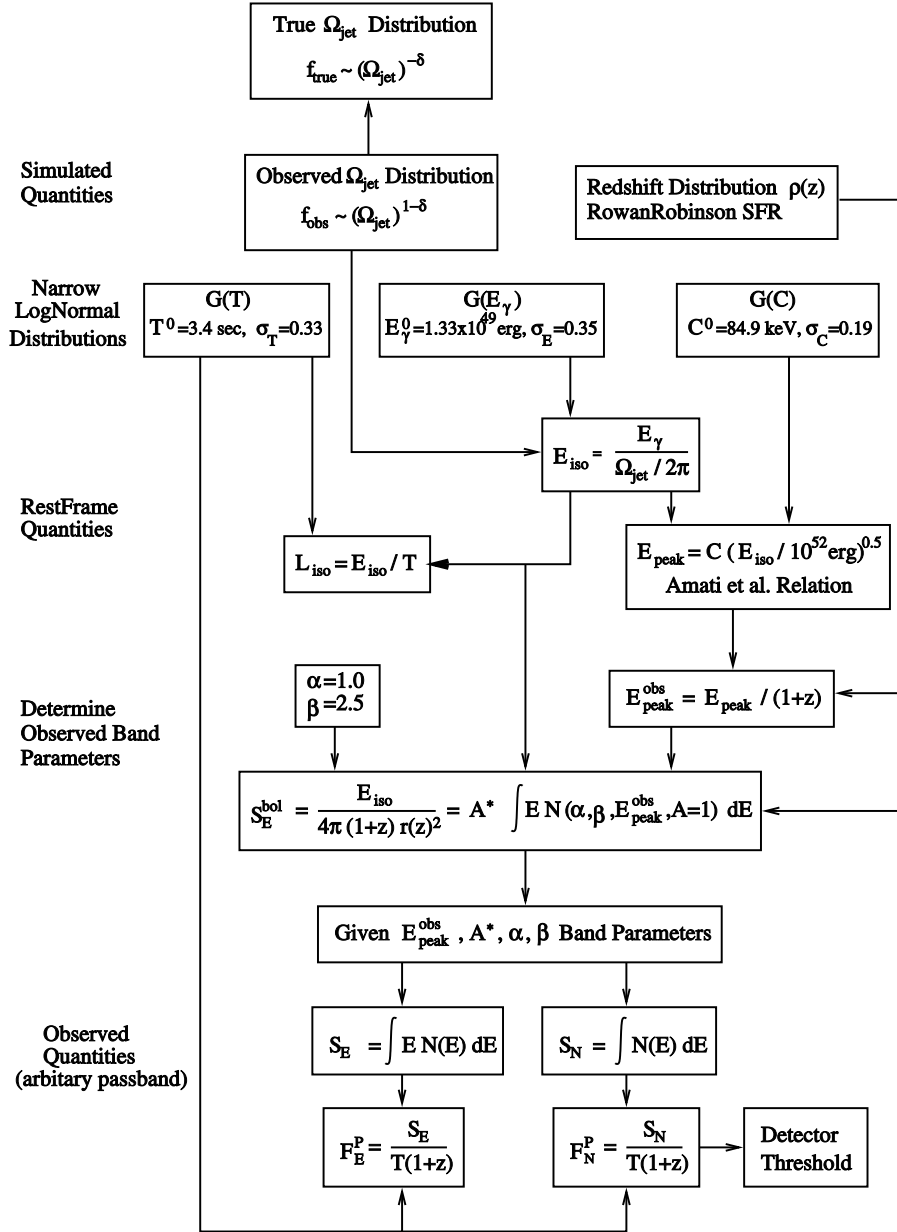$$E_{\rm iso} = \frac{E_\gamma}{C_{\rm jet}(\Omega_{\rm jet}/2\pi)}. \quad (8)$$

Fig. 6.—Flowchart showing the logical sequence of the simulations for the variable jet opening angle model.

XRF 020903, the dimmest burst in our sample, has $E_{\mathrm{iso}} = 2.3 \times 10^{49}$ ergs (Sakamoto et al. 2004a). Accounting for this burst requires that C_{jet} be at least 57.8; this choice is conservative in the sense that it implies that XRF 020903 lies at the faintest end of the range of possible values of E_{iso} and has the maximum possible opening angle of $\Omega_{\mathrm{jet}} = 2\pi$. The brightest burst in our sample is GRB 990123, which has $E_{\mathrm{iso}} = 2.8 \times 10^{54}$ ergs. Thus the range of E_{iso} is at least $\sim 10^5$, and so the range of Ω_{jet} must also be $\sim 10^5$. Since only E_{iso} is a directly observable quantity, the value of C_{jet} is degenerate with the value of the jet opening solid angle Ω_{jet}. Thus GRB 990123 provides a constraint only on $C_{\mathrm{jet}}\Omega_{\mathrm{jet}}^{\mathrm{min}}$.

Since we wish our burst simulations to explain the full range of observed E_{iso}, we require a range of approximately 5 decades in Ω_{jet} (conservatively, from 2π to $2\pi \times 10^{-5}$ sr). We have then varied C_{jet} to best match the observed cumulative distributions shown in Figure 14, as determined by visual comparison of the

observed and predicted cumulative distributions. The fiducial model that we use in this paper has a value of $C_{\mathrm{jet}} = 95$. This gives minimum and maximum values of E_{iso} of 1.4×10^{49} and 1.4×10^{54} ergs. The former value of E_{iso} implies a jet opening angle $\theta_{\mathrm{jet}} = 67°$ for XRF 020903 (the burst with the smallest value of E_{iso} in our sample). The latter value of E_{iso} is slightly smaller than the value of E_{iso} for GRB 990123 (the burst with the largest value of E_{iso} in our sample), but the range of simulated E_γ values, although narrow, is sufficient to account for this event and events like it. We have used the value $C_{\mathrm{jet}} = 95$ to rescale the Ω_{jet} values reported by Bloom et al. (2003) (see Fig. 12); this corresponds to making the coefficient in the relation between the jet break time and θ_{jet} a factor of ~ 10 smaller, and therefore the value of θ_{jet} a factor of ~ 10 smaller.

Thus the value of C_{jet} that we adopt in this paper requires that the value of θ_{jet} corresponding to a given jet break time be smaller than the value that is typically assumed by a factor of
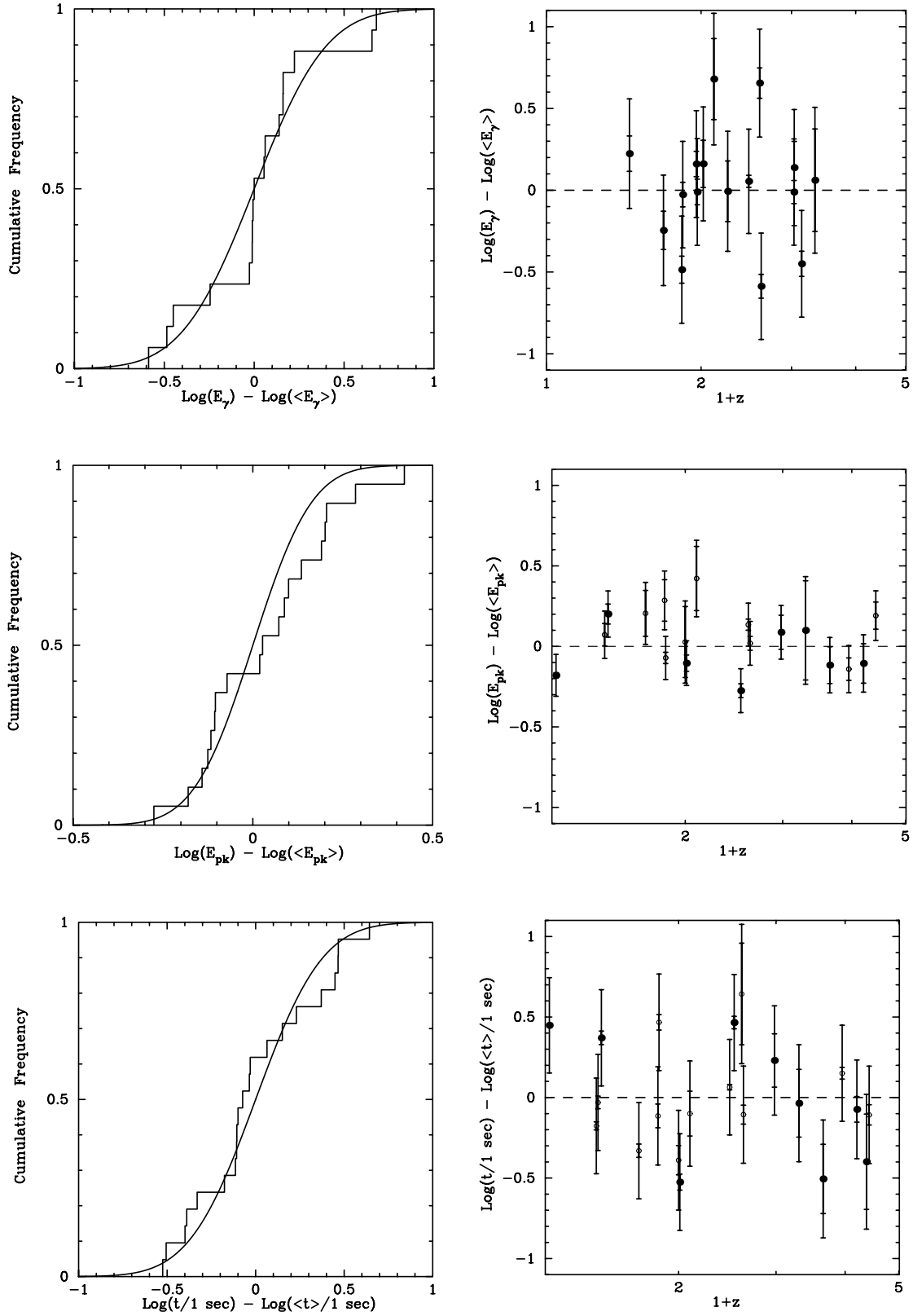
Fig. 7.—*Left*: Comparison of the best-fit smearing functions $G(E_\gamma)$, $G(C)$, and $G(T)$ and the cumulative distributions of E_γ (*top*), ΔE_{peak} (*middle*), and T_0 (*bottom*), respectively. *Right*: E_γ (*top*), the deviation ΔE_{peak} in E_{peak} of bursts from the E_{iso}-E_{peak} relation that we have adopted (*middle*), and $T_0 \sim F_N^P/S_E$ (*bottom*), as a function of redshift z. The smaller error bar represents the statistical error, while the larger represents the total error. Filled circles denote *HETE-2* points, while open circles denote *BeppoSAX* points. For more information see the text and Table 1.

TABLE 1
Parameters of Lognormal Distributions

Quantity	Central Value[a]	Sigma[a]	Source of Data
Energy radiated: $\log E_\gamma$ (ergs)	51.070 ± 0.095	$0.33^{+0.08}_{-0.06}$	1
$E_{\rm iso}$-$E_{\rm peak}$ relation: $\log C$ (keV)	1.950 ± 0.040	0.13	2, 3
Conversion timescale: $\log T$ (s)	0.574 ± 0.075	$0.305^{+0.062}_{-0.049}$	2, 3

[a] Lognormal distribution.
Sources.—(1) Bloom et al. 2003; (2) Amati et al. 2002; (3) Lamb et al. 2004d.

about 10, i.e., a factor of 2 more than the uncertainty stated by Sari et al. (1999). We return to this point below in § 6.

We incorporate the relation between $E_{\rm iso}$ and $E_{\rm peak}$ found by Amati et al. (2002) and extended by Lamb et al. (2004d), using a second narrow lognormal distribution, defined by

$$E_{\rm peak} = C \left(\frac{E_{\rm iso}}{10^{52} \text{ ergs}} \right)^s, \qquad (9)$$

$$G(C)d \log C = \exp\left[\frac{-(\log C - \log C_0)^2}{2\sigma_C^2} \right] d \log C. \qquad (10)$$

We set the power-law index $s = 0.5$. Then, using a full maximum likelihood approach to fit these equations to the *HETE-2* and *BeppoSAX* GRBs with known redshifts (see Figs. 2 and 7), we find maximum likelihood best-fit parameters $C_0 = 90.4$ keV and $\sigma_C = 0.70$ (see also Table 1). Again we find no evidence for any correlation of C with redshift (see Fig. 7). We therefore draw randomly from this Gaussian distribution to choose the value of $E_{\rm peak}$ corresponding to the value of $E_{\rm iso}$ for a particular burst.

Finally, we require the timescale that converts the isotropic-equivalent energy $E_{\rm iso}$ of a burst to the isotropic-equivalent peak luminosity $L_{\rm iso}$ of a burst. Using a full maximum likelihood approach, we determine this timescale by fitting a third narrow lognormal distribution, defined by

$$G(T)d \log T = \exp\left[\frac{-(\log T - \log T_0)^2}{2\sigma_T^2} \right] d \log T, \qquad (11)$$

to the distribution of the ratio $E_{\rm iso}/L_\gamma$ for the *HETE-2* and *BeppoSAX* bursts with known redshifts (see Fig. 7). Thus the timescale T is defined in the rest frame of the GRB source. We find maximum likelihood best-fit parameters $T_0 = 3.41$ s and $\sigma_T = 0.33$ (see also Table 1). Again, we find no evidence for any correlation of T with redshift (see Fig. 7). We therefore draw randomly from this Gaussian distribution and use the formula $L_{\rm iso} = E_{\rm iso}/T$ to convert $E_{\rm iso}$ to $L_{\rm iso}$, and thus also to convert burst fluences to peak fluxes. We note that the sample used for this fit also contains no XRFs.

4.2.2. *Power-Law Universal Jet Model*

Recovering the standard-energy result in the universal jet model requires $E_{\rm iso} \propto \theta_{\rm view}^{-2}$ (Rossi et al. 2002; Zhang & Mészáros 2002a; Perna et al. 2003). Therefore, in this paper we investigate a universal jet model in which the emissivity is a power-law function of the angle relative to the jet axis. In a subsequent paper (Donaghy et al. 2004a) we investigate a universal jet model in which the emissivity is a Gaussian function of the angle relative to the jet axis (Zhang et al. 2004a).

The requirement $E_{\rm iso} \propto \theta_{\rm view}^{-2} \propto \Omega_{\rm view}^{-1}$ allows us to simulate the power-law universal jet model by simply making the substitution $\Omega_{\rm jet} \rightarrow \Omega_{\rm view}$ in the variable jet opening angle simulations. To see this, compare equation (6) with the relation

$$E_{\rm iso} \propto \frac{1}{\theta_{\rm view}^2} \propto \frac{1}{\Omega_{\rm view}}. \qquad (12)$$

Although the physical interpretations of the two equations are entirely different, they give the same results. In addition to this substitution, we have to specify $\delta_{\rm sim}$ for the power-law universal jet model. Since the bursts are randomly oriented with respect to our line of sight, we draw $\Omega_{\rm view}$ values from a flat distribution, $d\Omega_{\rm view}$, which corresponds to $\delta_{\rm sim} = 0$. Drawing from this distribution results in very few small $\theta_{\rm view}$ values, compared to the very large number of $\theta_{\rm view}$ values near $\theta_{\rm view, max}$ (the angular extent of the universal jet) or $90°$, whichever is smaller. Therefore, in this model most bursts have $\theta_{\rm view} \sim \theta_{\rm view, max}$ or $90°$, whichever is smaller, and the range of observed $\Omega_{\rm view}$ values in logarithmic space is small for a finite sample of bursts. As a result, the power-law universal jet model predicts that most of the bursts arriving at the Earth will have small values of $E_{\rm iso}$, $L_{\rm iso}$, etc. (Rossi et al. 2002; Perna et al. 2003).

We also introduce the ability to rescale the central value of E_γ in the power-law universal jet model (see eq. [8]). For this model we consider two cases: in the first case, we "pin" the minimum value of $E_{\rm iso}$ (i.e., the value of $E_{\rm iso}$ corresponding to $\Omega_{\rm view} = 2\pi$) to the value of $E_{\rm iso}$ for XRF 020903; in the second case, we pin the minimum value of $E_{\rm iso}$ to the value of $E_{\rm iso}$ for GRB 980326 (the smallest $E_{\rm iso}$ in our sample of *HETE-2* and *BeppoSAX* bursts with known redshifts, apart from the XRFs). In the first case, we derive $C_{\rm jet} = 58$, and in the second $C_{\rm jet} = 0.24$. In the first case, the power-law universal jet model can then generate the full observed range of $E_{\rm iso}$ (i.e., both XRFs and GRBs), while in the second case, it can generate the range of $E_{\rm iso}$ values corresponding to GRBs, but not to XRFs or X-ray–rich GRBs.

4.3. *GRB Rate as a Function of Redshift*

The observed rate of GRBs per redshift interval dz is given by

$$\rho(z) = R_{\rm GRB}(z)(1+z)^{-1} 4\pi r(z)^2 \frac{dr}{dz} \quad (\text{number } dz^{-1} \text{ yr}^{-1}), \qquad (13)$$

where $R_{\rm GRB}(z)$ is the rate of GRBs per comoving volume and $r(z)$ is the comoving distance to the source [see § 4.3 below for the precise definition of $r(z)$]. We use the phenomenological parameterization of the star formation rate (SFR) as a function of redshift suggested by Rowan-Robinson (2001) to parameterize

the GRB rate as a function of redshift. In this parameterization, $R_{\rm GRB}$ is given by

$$R_{\rm GRB}(z)$$
$$= R_0 \left[\frac{t(z)}{t(0)} \right]^P \exp\left\{ Q\left[1 - \frac{t(z)}{t(0)} \right] \right\} \quad (\text{number yr}^{-1}\ \text{Gpc}^{-3}). \tag{14}$$

Here, $t(z)$ is the elapsed coordinate time since the big bang at that redshift. In this paper, we adopt the values $P = 1.2$ and $Q = 5.4$, which provide a good fit to existing data on the SFR as a function of redshift. The resulting curve of the SFR as a function of redshift is given in Figure 8. It rises rapidly from $z = 0$, peaks at $z \approx 1.5$, and then decreases gradually with increasing redshift. We draw GRB redshifts randomly from this SFR curve.

The actual SFR as a function of redshift is uncertain, and the GRB rate as a function of redshift is even more uncertain. Several studies have suggested that the GRB rate may be flat, or may even increase, at high redshifts (Fenimore & Ramirez-Ruiz 2000; Lloyd-Ronning et al. 2002; Reichart & Lamb 2001). The particular choice that we have made of the GRB rate as a function of redshift has little effect on the comparisons with observations that we carry out in this paper, since all of the bursts that we consider are at modest redshifts ($z \lesssim 3$). However, predictions of the fraction of bursts that lie at very high redshifts ($z > 5$), and therefore the number of detectable bursts at very high redshifts, are sensitive to the shape of the GRB rate curve at very high redshifts.

4.4. *Cosmology*

The Rowan-Robinson SFR model depends on a few basic cosmological parameters, as do the observed peak photon number and energy fluxes and fluences of the bursts. In this paper, we adopt the values $\Omega_M = 0.3$, $\Omega_\Lambda = 0.7$, and $H_0 = 65$ km s^{-1} Mpc^{-1}.

The comoving distance to redshift z is defined by

$$\frac{dr}{dz} = \frac{c}{H_0} \left[\Omega_k(1+z)^2 + \Omega_\Lambda + \Omega_M(1+z)^3 + \Omega_R(1+z)^4 \right]^{-1/2}, \tag{15}$$

and integrating this equation over dz gives us $r(z)$.

To calculate the time since the big bang we integrate the following formula:

$$dt = \frac{da}{a\,H_0} \left[\Omega_k a^{-2} + \Omega_\Lambda + \Omega_M a^{-3} + \Omega_R a^{-4} \right]^{-1/2}, \tag{16}$$

which yields an expression for $t(z)$. Here $a = (1+z)^{-1}$. For our adopted cosmology, there is an analytic expression for $t(z)$, which is

$$H_0 t(z) = \frac{2}{3\Omega_\Lambda^{1/2}} \sinh^{-1}\left[\left(\frac{\Omega_\Lambda}{\Omega_M} \right)^{1/2} (1+z)^{-3/2} \right], \tag{17}$$

but there is no analytic expression for $r(z)$.

4.5. *Observable Quantities*

In this paper, we assume that the spectra of GRBs are a Band function (Band et al. 1993) in which $\alpha = -1$, $\beta = -2.5$, and $E_{\rm peak}^{\rm obs} = E_{\rm peak}/(1+z)$. We have also done simulations assuming $\alpha = -0.5$ and -1.5 and $\beta = -2.0$ and -3.0; these different choices make little difference in our results.
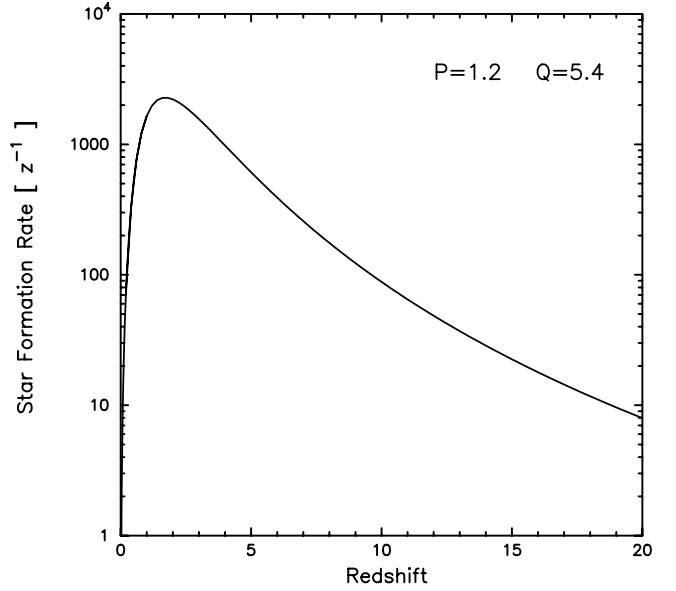

Fig. 8.—GRB rate as a function of redshift that we assume in this paper. The curve is the Rowan-Robinson (2001) function for the star formation rate (eq. [3]), taking $P = 1.2$ and $Q = 5.4$.

Given $E_{\rm iso}$, $E_{\rm peak}$, and T, we calculate $L_{\rm iso}^E = E_{\rm iso}/T$ and the normalization constant A of the Band spectrum in the rest frame of the burst source. We can then calculate the following peak fluxes and fluences:

$$F_E^P = \frac{L_{\rm iso}^E}{4\pi r^2(z)(1+z)^2} \quad (\text{ergs cm}^{-2}\ \text{s}^{-1}),$$
$$S_E = F_E^P T(1+z) \quad (\text{ergs cm}^{-2}); \tag{18}$$

$$F_N^P = \frac{L_{\rm iso}^N}{4\pi r^2(z)(1+z)} \quad (\text{photons cm}^{-2}\ \text{s}^{-1}),$$
$$S_N = F_N^P T(1+z) \quad (\text{photons cm}^{-2}). \tag{19}$$

However, these are bolometric quantities, not observed quantities; in order to calculate the observed peak fluxes and fluences, we must model the instruments.

Given $E_{\rm iso}$, $E_{\rm peak}$, and z from the simulations, we calculate the normalization constant A^* of the Band function by considering the bolometric fluence as observed in our reference frame:

$$S_E^{\rm bol} = \frac{E_{\rm iso}}{4\pi(1+z)r(z)^2} = A^* \int_0^\infty EN(E;\ \alpha,\ \beta,\ E_{\rm peak}^{\rm obs},\ A=1)\,dE. \tag{20}$$

Once we have A^*, we can calculate the observed fluxes and fluences in the passband of our instrument:

$$S_E^{\rm obs} = \int_{\rm inst} EN(E;\ \alpha,\ \beta,\ E_{\rm peak}^{\rm obs},\ A^*)\,dE, \quad F_E^{P,\rm obs} = \frac{S_E^{\rm obs}}{T(1+z)}; \tag{21}$$

$$S_N^{\rm obs} = \int_{\rm inst} N(E;\ \alpha,\ \beta,\ E_{\rm peak}^{\rm obs},\ A^*)\,dE, \quad F_N^{P,\rm obs} = \frac{S_N^{\rm obs}}{T(1+z)}. \tag{22}$$

To determine whether a particular burst will be detected by a particular instrument, we define the efficiency as a function of E_{peak}^{obs},

$$\epsilon\left(E_{peak}^{obs}\right) = \frac{\int_{inst} N(E; \alpha, \beta, E_{peak}^{obs}, A^*)\, dE}{\int_{0.1}^{10000} N(E; \alpha, \beta, E_{peak}^{obs}, A^*)\, dE} = \frac{F_N^{P, inst}}{F_N^{P, \oplus}}, \quad (23)$$

where $F_N^{P, \oplus}$ and $F_N^{P, inst}$ are the bolometric peak photon number flux of the burst at the Earth and the peak photon number flux of the burst as measured by a particular instrument, respectively. This expression gives a shape function that we normalize to Figures 2–9 of Band (2003) for the desired detector. Note that our shape function is the same as Band's, except that we consider incident burst spectra extending from 0.1 to 10000 keV instead of from 1 to 1000 keV, in order to encompass the full range of values of E_{peak}^{obs} observed by *HETE-2* for XRFs, X-ray–rich GRBs, and GRBs.

The normalization is approximately given by

$$D_{inst} = \frac{C_{min}(\sigma, B)}{A_{eff} \Delta t_{trig}} \quad \text{(photons s}^{-1}\text{ cm}^{-2}\text{)}, \quad (24)$$

where $C_{min}(\sigma, B)$ is the minimum detectable number of counts in the detector, σ is the supernova rate (SNR) required for detection, B is the background count rate from the diffuse X-ray background, A_{eff} is the effective area of the detector, and Δt_{trig} is the trigger timescale (Band 2003). A burst is detected if

$$F_N^{P, \oplus} \geq \frac{D_{inst}}{\epsilon(E_{peak}^{obs})} = F_{N, min}^{P, \oplus}, \quad \text{i.e., } F_N^{P, inst} \geq D_{inst} = F_{N, min}^{P, inst}. \quad (25)$$

Thus D_{inst} is the peak number flux detection threshold in the instrument passband.

We have reproduced the results of Band (2003) for BATSE on the *Compton Gamma Ray Observatory*, the WFC and GRBM on *BeppoSAX*, and the WXM and FREGATE on *HETE-2*. However, we use a trigger timescale $\Delta t_{trig} = 5$ s for the WXM on *HETE-2*, rather than the value of 1 s used by Band (2003). We also use a threshold SNR for detection of a burst by the GRBM on *BeppoSAX* of 15 (E. Costa & F. Frontera 2003, private communication), rather than the value of 5.6 used by Band (2003).[2]

Figure 9 shows the threshold sensitivity curves in peak photon number flux F_N^P for the WXM and FREGATE on *HETE-2* and for the WFC and GRBM on *BeppoSAX* as a function of E_{peak}^{obs}, the observed peak energy of the νF_ν spectrum of the burst. Since *BeppoSAX* could not trigger on WFC data and was forced to rely on the less-sensitive GRBM for its triggers, we consider a burst to have been detected by *BeppoSAX* only if its peak flux

falls above the GRBM sensitivity threshold. Since *HETE-2* can trigger on WXM data, we consider a burst to have been detected if its peak flux falls above the minimum of the WXM and FREGATE sensitivity thresholds. These bursts form the ensemble of observed bursts from which we construct various observed distributions.

5. RESULTS

The data sets for S_E and E_{peak}^{obs}, and especially for E_{iso} and E_{peak} (which require knowledge of the redshift of the burst), are sparse at the present time. The latter two data sets also suffer from a large observational selection effect (there is a dearth of XRFs with known redshifts because the X-ray and optical afterglows of XRFs are so faint). In addition, the K-S test (which is the appropriate test to use to compare cumulative distributions) is notoriously weak. We therefore do not think that it is justified to carry out detailed fits to these data sets at this time; in fact, we think that doing so is likely to produce highly misleading results. We have therefore contented ourselves with making fits to these data sets "by eye," which can support qualitative— but not quantitative—conclusions.

In comparing the observed properties of XRFs, X-ray–rich GRBs, and GRBs, and their predicted properties in the variable jet opening angle model, we consider values of the power-law index for the distribution of jet solid angles Ω_{jet} of $\delta = 1, 2,$ and 3. As we will see, the observed properties of the bursts are fitted best by $\delta = 2$, which implies approximately equal numbers of bursts per logarithmic interval in all observed quantities.

In comparing the observed properties of XRFs, X-ray–rich GRBs, and GRBs, and their predicted properties in the power-law universal jet model, we adopt $E_{iso} \propto \Omega_{view}^{-1}$ since this relation is required in order to recover the standard-energy result for GRBs. In addition, we consider two possibilities for the range of Ω_{view}. In the first case, we require the power-law universal jet model to account for the full range of the E_{iso}-E_{peak} relation, including XRFs, X-ray–rich GRBs, and GRBs; i.e., we fix the normalization of E_γ^0 so that the smallest value of E_{iso} given by the model is the value of E_{iso} for XRF 020903. In the second case, we fix the normalization of E_γ^0 so that the smallest value of E_{iso} given by the model is the E_{iso} value for GRB 980326, the GRB with the smallest E_{iso} in the *BeppoSAX* sample.

Figure 9 shows the detectability of bursts by *HETE-2* and *BeppoSAX* in the variable jet opening angle model for $\delta = 2$. Detected bursts are shown in blue and nondetected bursts in red. The left-hand panels show bursts in the (E_{iso}, E_{peak})-plane detected by *HETE-2* (*top*) and by *BeppoSAX* (*bottom*). For each experiment, we overplot the locations of the *HETE-2* and *BeppoSAX* bursts with known redshifts. The observed burst in the lower left-hand corner of the *HETE-2* panel is XRF 020903, the most extreme burst in our sample. The agreement between the observed and predicted distributions of bursts is good. The right-hand panels show bursts in the $[E_{peak}^{obs}, F_N^P(0.1$–$10000 \text{ keV})]$-plane detected by *HETE-2* (*top*) and by *BeppoSAX* (*bottom*). For each experiment we show the sensitivity thresholds for their respective instruments plotted in solid blue. The BATSE threshold is shown in both panels as a dashed blue line. Again, the agreement between the observed and predicted distributions of bursts is good. The left-hand panels exhibit the constant density of bursts per logarithmic interval in E_{iso} and E_{peak} given by the variable jet opening angle model for $\delta = 2$. Since $L_{iso} = E_{iso}/T$, this choice of $\delta = 2$ corresponds to a GRB luminosity function $f(L_{iso}) \propto L_{iso}^{-1}$, which is roughly consistent with those found by Schmidt (2001) and Lloyd-Ronning et al. (2002).

---

[2] The reason for this is the following: The half-opening angle of the WFC is $\theta_{WFC} = 20°$. The GRBM consists of four anti-coincidence shields, two of which are normal to the WFC boresight and two of which are parallel to it. In order to be detected, a burst must be detected in at least two of the anti-coincidence shields; i.e., it must exceed 5 σ in one of the two anti-coincidence shields that are normal to the WFC boresight *and* in one of the two anti-coincidence shields that are parallel to the WFC boresight. A burst that exceeds 5 σ in one of the two anti-coincidence shields that are parallel to the WFC boresight and is localized by the WFC (i.e., that lies within 20° of the WFC boresight) exceeds 25 σ in the anti-coincidence shield that is normal to the WFC boresight. Detailed Monte Carlo simulations show that some of a burst's gamma rays are scattered by material in the WFC into one or the other of the two anti-coincidence shields that are parallel to the WFC boresight. This reduces the required SNR of the burst in the anti-coincidence shield that is normal to the WFC boresight to ≈ 15 σ (E. Costa & F. Frontera 2003, private communication).
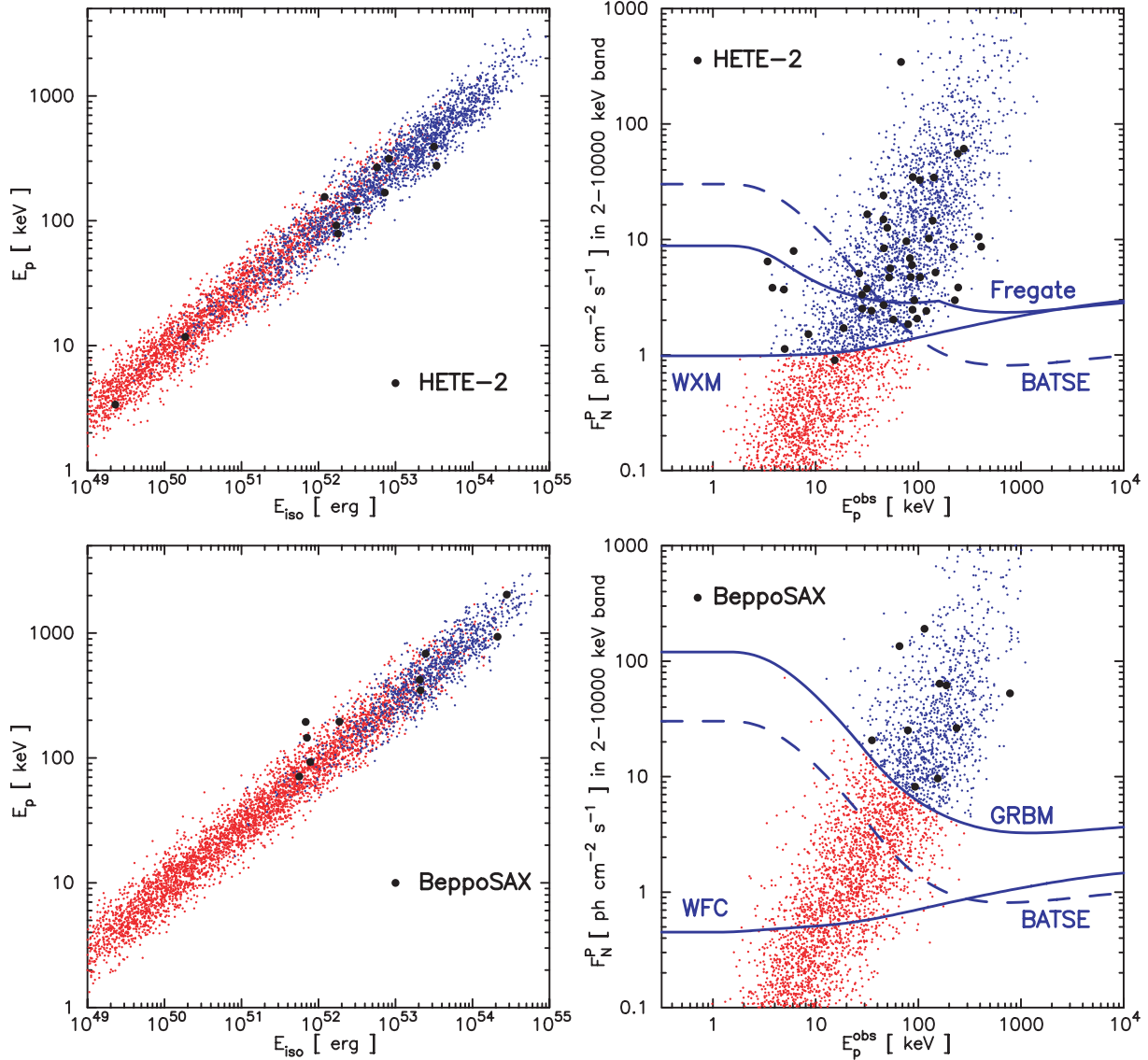
Fig. 9.—Comparison of the detectability of bursts by *HETE-2* and *BeppoSAX* in the variable jet opening angle model for $\delta = 2$. Detected bursts are shown in blue and nondetected bursts in red. The left-hand panels show bursts in the (E_{iso}, E_{peak})-plane detected by *HETE-2* (*top*) and by *BeppoSAX* (*bottom*). For each experiment, we overplot the locations of the *HETE-2* and *BeppoSAX* bursts with known redshifts. The observed burst in the lower left-hand corner of the *HETE-2* panel is XRF 020903, the most extreme burst in our sample. The agreement between the observed and predicted distributions of bursts is good. The right-hand panels show bursts in the $[E_{peak}^{obs}, F_N^P(2-10000\ keV)]$-plane detected by *HETE-2* (*top*) and by *BeppoSAX* (*bottom*). For each experiment we show the sensitivity thresholds for their respective instruments plotted as solid blue lines. The BATSE threshold is shown in both panels as a dashed blue line. Again, the agreement between the observed and predicted distributions of bursts is good. The left-hand panels exhibit the constant density of bursts per logarithmic interval in E_{iso} and E_{peak} given by the variable jet opening angle model for $\delta = 2$.

Figure 10 shows scatter plots of S_E and S_N versus Ω_{jet}. The top panels show the predicted distributions in the variable jet model for $\delta = 2$, while the bottom panels show the power-law universal jet opening angle model pinned to the E_{iso} value of XRF 020903. Detected bursts are shown in blue and nondetected bursts in red. The top panels exhibit the constant density of bursts per logarithmic interval in S_E, S_N, and Ω_{jet} given by the variable jet opening angle model for $\delta = 2$. The bottom panels exhibit the concentration of bursts at $\Omega_{jet} \equiv \Omega_{view} \approx 2\pi$ and the resulting preponderance of XRFs relative to GRBs in the power-law universal jet model when it is pinned to the E_{iso} value of XRF 020903, i.e., when one attempts to extend the model to include XRFs and X-ray–rich GRBs, as well as GRBs.

Figure 11 shows scatter plots of F_E^P and F_N^P versus Ω_{jet}. The top panels show the predicted distributions in the variable jet

opening angle model for $\delta = 2$, while the middle and the bottom panels show the power-law universal jet model pinned to the E_{iso} values of XRF 020903 and GRB 980326, respectively. In these scatter plots, as in the other scatter plots presented in this paper, we show a random subsample (usually 5000 bursts) of the 50,000 bursts that we have generated. Detected bursts are shown in blue and non-detected bursts in red. The top panels exhibit the constant density of bursts per logarithmic interval in F_E^P, F_N^P, and Ω_{jet} given by the variable jet opening angle model for $\delta = 2$. The middle and bottom panels show the concentration of bursts at $\Omega_{jet} \equiv \Omega_{view} \approx 2\pi$. The middle panels show the resulting preponderance of XRFs relative to GRBs in the power-law universal jet model when it is pinned to the E_{iso} values of XRF 020903, i.e., when one attempts to extend the model to include XRFs and X-ray–rich GRBs, as well as GRBs.
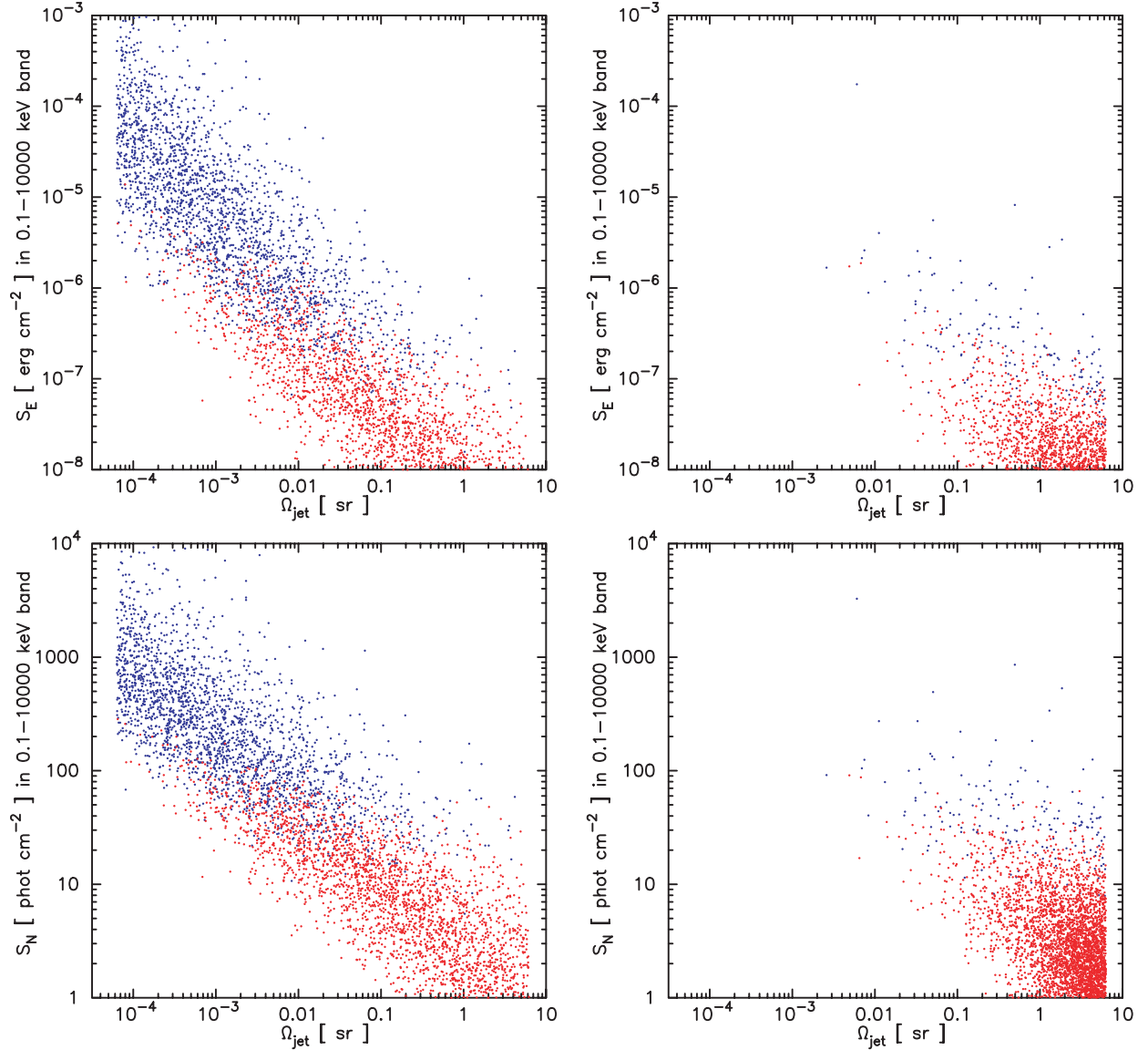
Fig. 10.—Scatter plots of S_E and S_N vs. $\Omega_{\rm jet}$. The top panels show the predicted distributions in the variable jet opening angle model for $\delta = 2$, while the bottom panels show the power-law universal jet model pinned to the $E_{\rm iso}$ value of XRF 020903 (see text). Bursts detected by the WXM are shown in blue and nondetected bursts in red. The top panels exhibit the constant density of bursts per logarithmic interval in S_E, S_N, and $\Omega_{\rm jet}$ given by the variable jet opening angle model for $\delta = 2$. The bottom panels exhibit the concentration of bursts at $\Omega_{\rm jet} \equiv \Omega_{\rm view} \approx 2\pi$ and the resulting preponderance of XRFs relative to GRBs in the power-law universal jet model when it is pinned to the $E_{\rm iso}$ value of XRF 020903, i.e., when one attempts to extend the model to include XRFs and X-ray–rich GRBs, as well as GRBs.

Figure 12 shows the observed and predicted cumulative distributions of $\Omega_{\rm jet}$. The left panel shows the cumulative distributions of $\Omega_{\rm jet}$ predicted by the variable jet opening angle model for $\delta = 1$, 2, and 3 (solid curves), compared to the observed cumulative distribution of the values of $\Omega_{\rm jet}$ given in Bloom et al. (2003) scaled downward by a factor of $C_{\rm jet} = 95$ (solid histogram). The predicted cumulative distribution of $\Omega_{\rm jet}$ given by $\delta = 2$ fits the shape and values of the scaled $\Omega_{\rm jet}$ distribution reasonably well. The right panel shows the cumulative $\Omega_{\rm jet} \equiv \Omega_{\rm view}$ distributions predicted by the power-law universal jet model with the minimum value of $E_{\rm iso}$ pinned to the value of $E_{\rm iso}$ for XRF 020903 (solid curve) and to the value of $E_{\rm iso}$ for GRB 980326 (dashed curve) These models are compared with the observed cumulative distribution of the values of $\Omega_{\rm jet}$ given in Bloom et al. (2003) (dashed histogram) and the same distribution scaled downward by a factor of $C_{\rm jet} = 95$ (solid histogram). The cumulative $\Omega_{\rm jet}$ distribution predicted by the power-law universal jet model pinned to GRB 9980326 fits the

shape and values of the observed cumulative distribution given by the values of $\Omega_{\rm jet}$ in Bloom et al. (2003) reasonably well if the observed values are scaled upward by a factor of ≈ 7. The cumulative distribution of $\Omega_{\rm jet}$ predicted by the power-law universal jet model pinned to XRF 020903 does not fit the shape of the observed cumulative distribution of $\Omega_{\rm jet}$ for any scaling factor.

Figure 13 shows scatter plots of $E_{\rm iso}$ versus $E_{\rm peak}$ (left) and $E_{\rm peak}$ versus S_E (right). The top panels show the predicted distributions in the variable jet opening angle model for $\delta = 2$, while the middle and the bottom panels show the power-law universal jet model pinned to the $E_{\rm iso}$ values of XRF 020903 and GRB 980326, respectively. Detected bursts are shown in blue and nondetected bursts in red. In the left column, the black triangles and circles show the locations of the *BeppoSAX* and *HETE-2* bursts with known redshifts. In the right column, the black circles show the locations of *HETE-2* bursts for which joint fits to WXM and FREGATE spectral data have been carried out (Sakamoto et al. 2004b). The top panels exhibit the
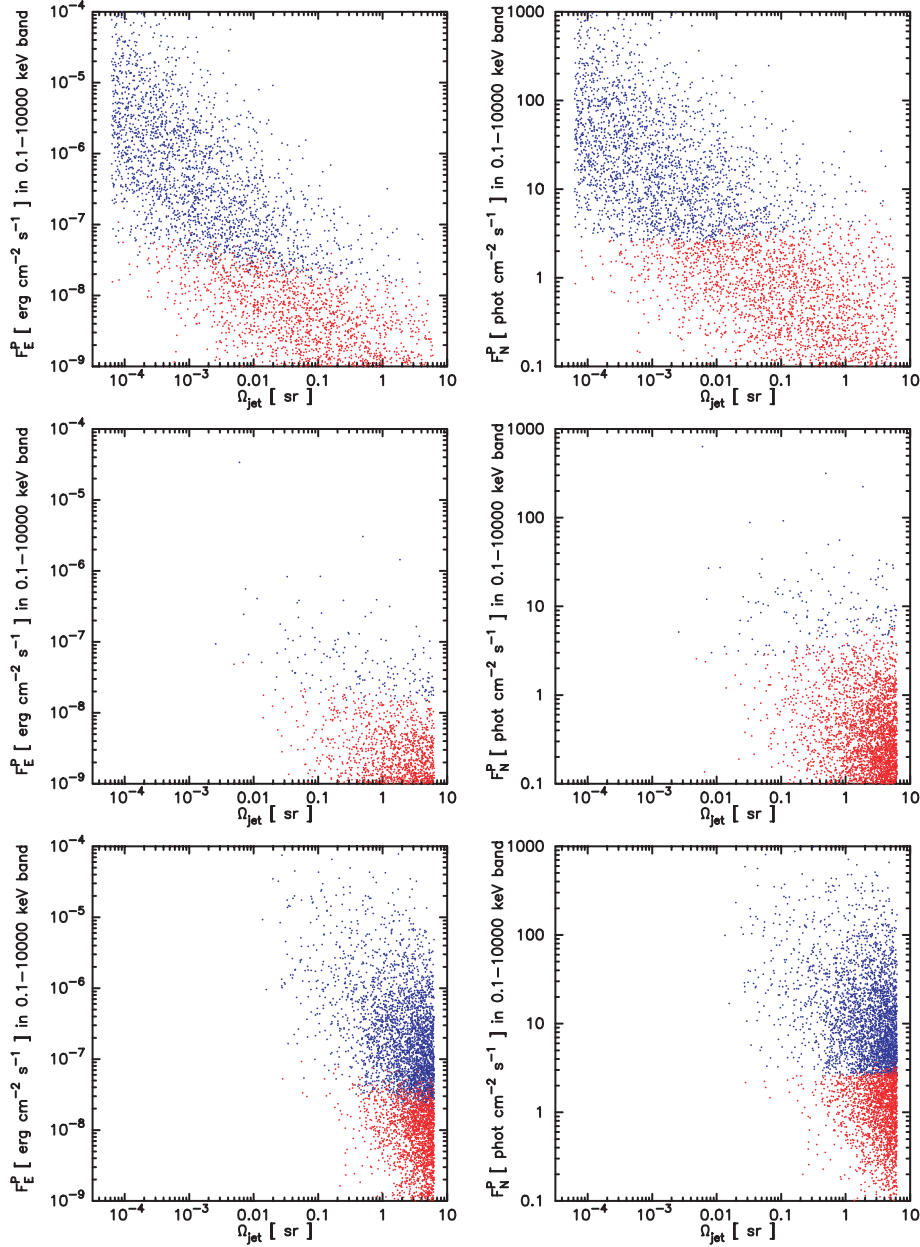
Fig. 11.—Scatter plots of F_E^P and F_N^P vs. $\Omega_{\rm jet}$. The top panels show the predicted distributions in the variable jet opening angle model for $\delta = 2$, while the middle and the bottom panels show the power-law universal jet model pinned to the $E_{\rm iso}$ values of XRF 020903 and GRB 980326, respectively (see text). Bursts detected by the WXM are shown in blue and nondetected bursts in red.

constant density of bursts per logarithmic interval in $E_{\rm iso}$, $E_{\rm peak}$, and S_E given by the variable jet opening angle model for $\delta = 2$. The middle and bottom panels show the limited range in $E_{\rm iso}$, $E_{\rm peak}$, and S_E of detected bursts in the power-law universal jet model. The middle panels show the preponderance of XRFs relative to GRBs predicted in the power-law universal jet model when it is pinned to the $E_{\rm iso}$ value of XRF 020903, i.e., when one attempts to extend the model to include XRFs and X-ray–rich GRBs, as well as GRBs.

Figure 14 compares the observed and predicted cumulative distributions of $E_{\rm iso}$ and $E_{\rm peak}$ for *BeppoSAX* and *HETE-2* bursts with known redshifts, and the observed and predicted cumulative distributions of S_E and $E_{\rm peak}^{\rm obs}$ for all *HETE-2* bursts. The solid histograms are the observed cumulative distributions. The solid curves are the cumulative distributions predicted by the variable jet opening angle model for $\delta = 2$. The dotted

curves are the cumulative distributions predicted by the power-law universal jet model pinned at the $E_{\rm iso}$ value of XRF 020903, i.e., when one attempts to extend the model to include XRFs and X-ray–rich GRBs, as well as GRBs. The dashed curves are the cumulative distributions predicted by the power-law universal jet model pinned at the $E_{\rm iso}$ value of GRB 980326, i.e., when one fits the model only to GRBs. The cumulative distributions in the present figure correspond to those formed by projecting the observed and predicted distributions in Figure 13 onto the x- and y-axes of the panels in that figure. The present figure shows that the variable jet opening angle model for $\delta = 2$ can explain the observed distributions of burst properties reasonably well, especially given that the sample of XRFs with known redshifts is incomplete due to optical observational selection effects (see § 6.6.1). It also shows that the power-law universal jet model can explain the observed distributions of GRB properties reasonably
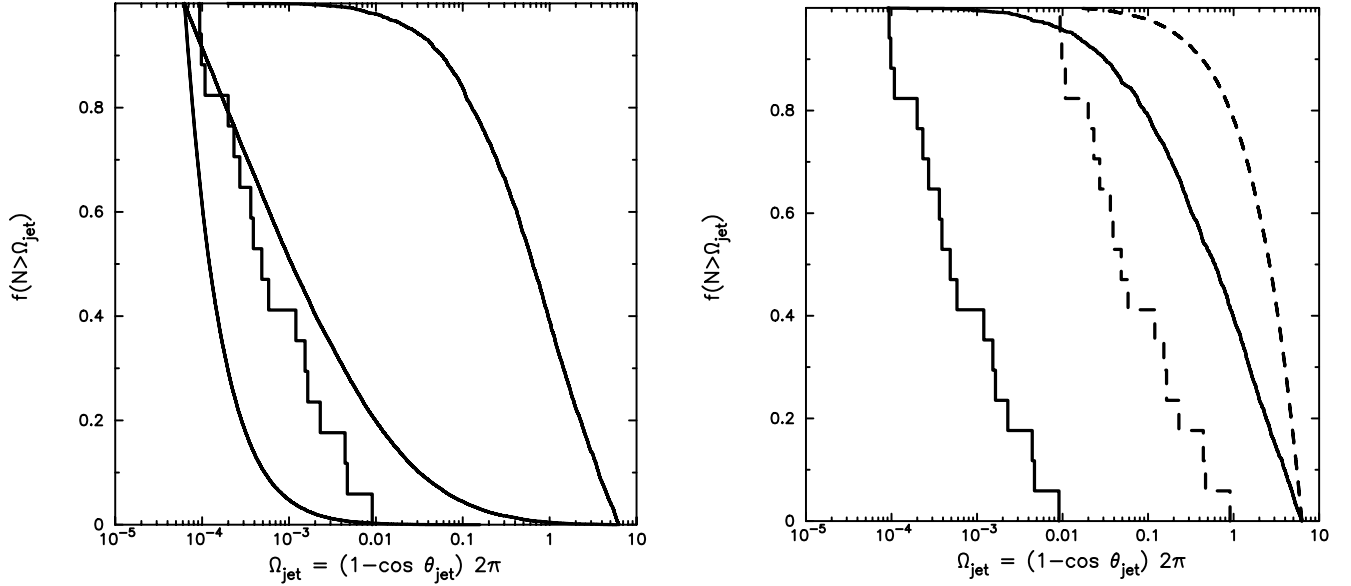
Fig. 12.—Observed and predicted cumulative distributions of Ω_{jet}. *Left*: Cumulative distributions of Ω_{jet} predicted by the variable jet opening angle model for $\delta = 1$, 2, and 3 (*curves from right to left*), compared to the observed cumulative distribution of the values of Ω_{jet} given in Bloom et al. (2003) scaled downward by a factor of $C_{jet} = 95$ (*solid histogram*). *Right*: Cumulative $\Omega_{jet} \equiv \Omega_{view}$ distributions predicted by the power-law universal jet model with the minimum value of E_{iso} pinned to the value of E_{iso} for XRF 020903 (*solid curve*) and to the value of E_{iso} for GRB 980326 (*dashed curve*). Models are compared with observed cumulative distribution of the values of Ω_{jet} given in Bloom et al. (2003) (*dashed histogram*) and the same scaled downward by a factor of $C_{jet} = 95$ (*solid histogram*). See the text for more details.

well, but cannot do so if asked to explain the properties of XRFs and X-ray–rich GRBs, as well as GRBs.

Figure 15 shows scatter plots of F_N^P (*left*) and E_{peak}^{obs} (*right*) as a function of redshift. The top panels show the distributions of bursts predicted by the variable jet opening angle model for $\delta = 2$. The middle panels show the distributions of bursts predicted by the power-law universal jet model pinned to the E_{iso} value for XRF 020903, while the bottom panels show the distributions of bursts predicted by the power-law universal jet model pinned to the E_{iso} value for GRB 980326. Detected bursts are shown in blue and nondetected bursts in red. The black circles show the positions of the *HETE-2* bursts with known redshifts. This figure shows that variable jet opening angle model for $\delta = 2$ can explain the observed distributions of bursts in the $(1+z, F_N^P)$- and $(1+z, E_{peak}^{obs})$-planes reasonably well. It also shows that the power-law universal jet model can explain the observed distributions of GRBs alone reasonably well, but cannot explain the observed distributions of XRFs, X-ray–rich GRBs, and GRBs. These conclusions are confirmed by Table 2, which shows the percentages of XRFs, X-ray–rich GRBs, and hard GRBs in the *HETE-2* data and predicted by the variable jet opening angle model and the power-law universal jet model.

Figure 16 shows scatter plots of L_{iso} versus E_{peak} and a comparison of the observed and predicted cumulative distributions of L_{iso}. The top left panel shows the distribution of bursts predicted by the variable jet opening angle model for $\delta = 2$. The bottom left panel shows the distribution of bursts predicted by the power-law universal jet model pinned at the E_{iso} value for XRF 020903. The bottom right panel shows the power-law universal jet model pinned at the E_{iso} value for GRB 980326. Detected bursts are shown in blue and nondetected bursts in red. The black circles show the positions of the *HETE-2* bursts with known redshifts. The top right panel shows the observed cumulative distribution of L_{iso} for *HETE-2* bursts with known redshifts (*histogram*) compared with the cumulative L_{iso} distribution predicted by the variable jet opening angle model for $\delta = 2$ (*solid curve*) and the cumulative L_{iso} distributions pre-

dicted by the power-law universal jet model pinned at the E_{iso} value for XRF 020903 (*dotted curve*) and for GRB 980326 (*dashed curve*). The figure shows that the variable jet opening angle model for $\delta = 2$ can explain the observed cumulative distributions of bursts in the (L_{iso}, E_{peak})-plane reasonably well. It also shows that the power-law universal jet model can explain the observed distribution of L_{iso} for GRBs alone reasonably well, but cannot explain the observed distribution for XRFs, X-ray–rich GRBs, and GRBs.

The left panel of Figure 17 shows the observed cumulative distribution of F_E^P for *HETE-2* bursts (*histogram*) compared with the cumulative F_E^P distribution predicted by the variable jet opening angle model for $\delta = 2$ (*solid curve*) and the cumulative F_E^P distributions predicted by the power-law universal jet model pinned at the E_{iso} value for XRF 020903 (*dotted curve*) and for GRB 980326 (*dashed curve*). This figure shows that variable jet opening angle model for $\delta = 2$ can explain the observed cumulative distribution of F_E^P for *HETE-2* bursts reasonably well. It also shows that the power-law universal jet model can explain the observed cumulative distribution of F_E^P for GRBs alone reasonably well, but cannot explain the observed distribution for XRFs, X-ray–rich GRBs, and GRBs seen by *HETE-2*. All three models have some difficulty explaining the cumulative F_E^P distribution for BATSE bursts (Donaghy et al. 2004b). The right panel of Figure 17 shows the differential distribution of E_{peak}^{obs} predicted by the variable jet opening angle model for $\delta = 2$ for bursts with $F_E^P > 10^{-8}$ (*solid histogram*), 10^{-7} (*dashed histogram*), and 10^{-6} ergs cm^{-2} s^{-1} (*dotted histogram*). The last distribution is in rough agreement with that found by Preece et al. (2000) for BATSE bursts with $F_E^P \gtrsim 5 \times 10^{-7}$ ergs cm^{-2} s^{-1} and $S_E > 4 \times 10^{-5}$ ergs cm^{-2}.

6. DISCUSSION

6.1. *Structure of GRB Jets*

Figures 13–16 show that the variable jet opening angle model with $\delta = 2$ can explain a number of the observed properties of
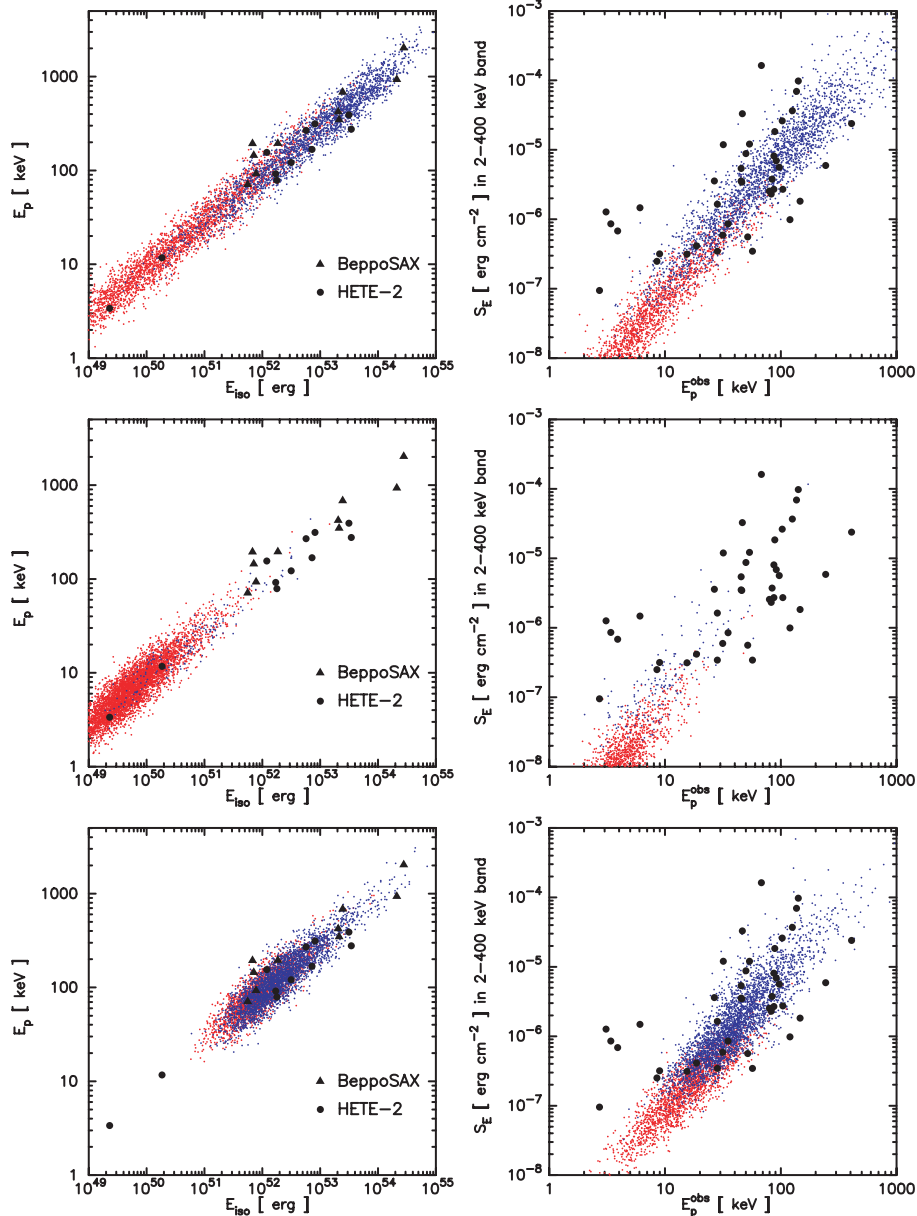
Fig. 13.—Scatter plots of E_{iso} vs. E_{peak} (*left*) and E_{peak} vs. S_E (*right*). The top panels show the predicted distributions in the variable jet opening angle model for $\delta = 2$, while the middle and the bottom panels show the power-law universal jet model pinned to the E_{iso} values of XRF 020903 and GRB 980326, respectively (see text). Bursts detected by the WXM are shown in blue, and nondetected bursts in red. In the left column, the triangles and circles respectively show the locations of the *BeppoSAX* and *HETE-2* bursts with known redshifts. In the right column, the black circles show the locations of all *HETE-2* bursts for which joint fits to WXM and FREGATE spectral data have been carried out (Sakamoto et al. 2004b).

GRBs reasonably well. These figures show that the power-law universal jet model (Rossi et al. 2002; Zhang & Mészáros 2002a; Mészáros et al. 2002; Perna et al. 2003; Zhang et al. 2004b) with $E_{iso} \propto \theta_{view}^{-2} \propto \Omega_{view}^{-1}$ (Zhang & Mészáros 2002a; Rossi et al. 2002; Perna et al. 2003) can also explain a number of the observed properties of GRBs reasonably well (see also Rossi et al. 2002; Perna et al. 2003).

However, as we have seen, *HETE-2* has provided strong evidence that the properties of XRFs, X-ray–rich GRBs, and GRBs form a continuum in the (E_{iso}, E_{peak})-plane (Lamb et al. 2004d) and in the (S_E, E_{peak}^{obs})-plane (Sakamoto et al. 2004b), and therefore that these three kinds of bursts are the same phenomenon. If this is true, it implies that the E_γ inferred by Frail et al. (2001), Panaitescu & Kumar (2001), and Bloom et al. (2003) is too large by a factor of at least 100. The reason is that

the values of E_{iso} for XRF 020903 (Sakamoto et al. 2004a) and XRF 030723 (Lamb et al. 2004d) are ~ 100 times smaller than the value of E_γ inferred by Frail et al. (2001) and Panaitescu & Kumar (2001)—an impossibility.

Motivated by the *HETE-2* results, we have explored in this paper the possibility of a unified jet model of XRFs, X-ray–rich GRBs, and GRBs. The *HETE-2* results show that S_E and E_{iso} decrease by a factor of $\sim 10^5$ in going from GRBs to XRFs (see Figs. 1 and 2). Figures 13–16 show that the variable jet opening angle model can accommodate the large observed ranges in S_E and E_{iso} reasonably well, while the power-law universal jet model cannot.

The reason is that the predictions of the variable jet opening angle and power-law universal jet models differ dramatically if they are required to accommodate the large observed ranges in
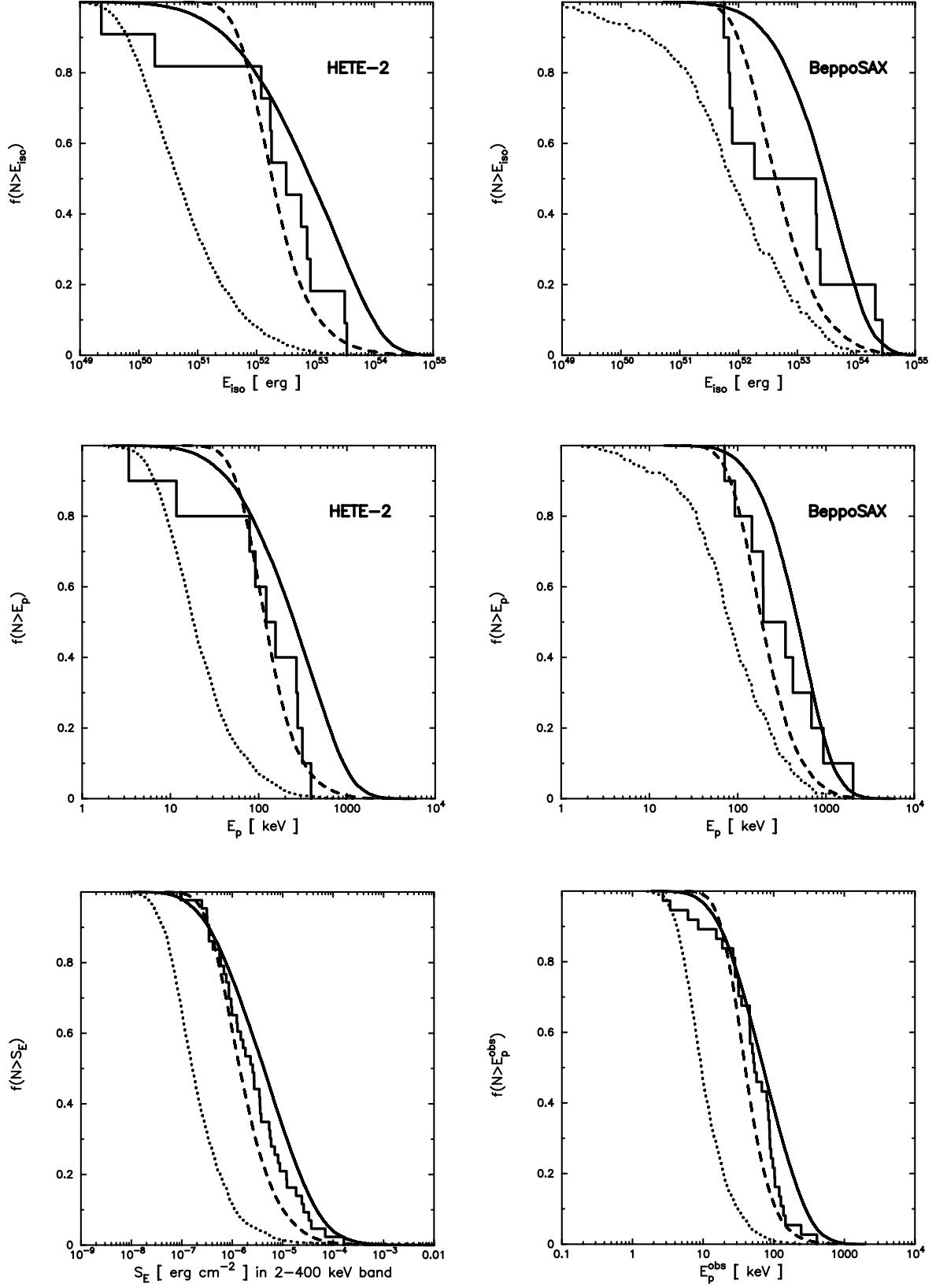
Fig. 14.—Comparison of the observed and predicted cumulative distributions of E_{iso} (*top*) and E_{peak} (*middle*) for *HETE-2* and *BeppoSAX* bursts with known redshifts, and of S_E and E_{peak}^{obs} for all *HETE-2* bursts (*bottom*). The solid histograms are the observed cumulative distributions. The blue curves are the cumulative distributions predicted by the variable jet opening angle model for $\delta = 2$. The solid red curves are the cumulative distributions predicted by the power-law universal jet model pinned at the E_{iso} value of XRF 020903, i.e., when one attempts to extend the model to include XRFs and X-ray–rich GRBs, as well as GRBs. The dashed red curves are the cumulative distributions predicted by the power-law universal jet model pinned at the E_{iso} value of GRB 980326, i.e., when one fits the model only to GRBs.
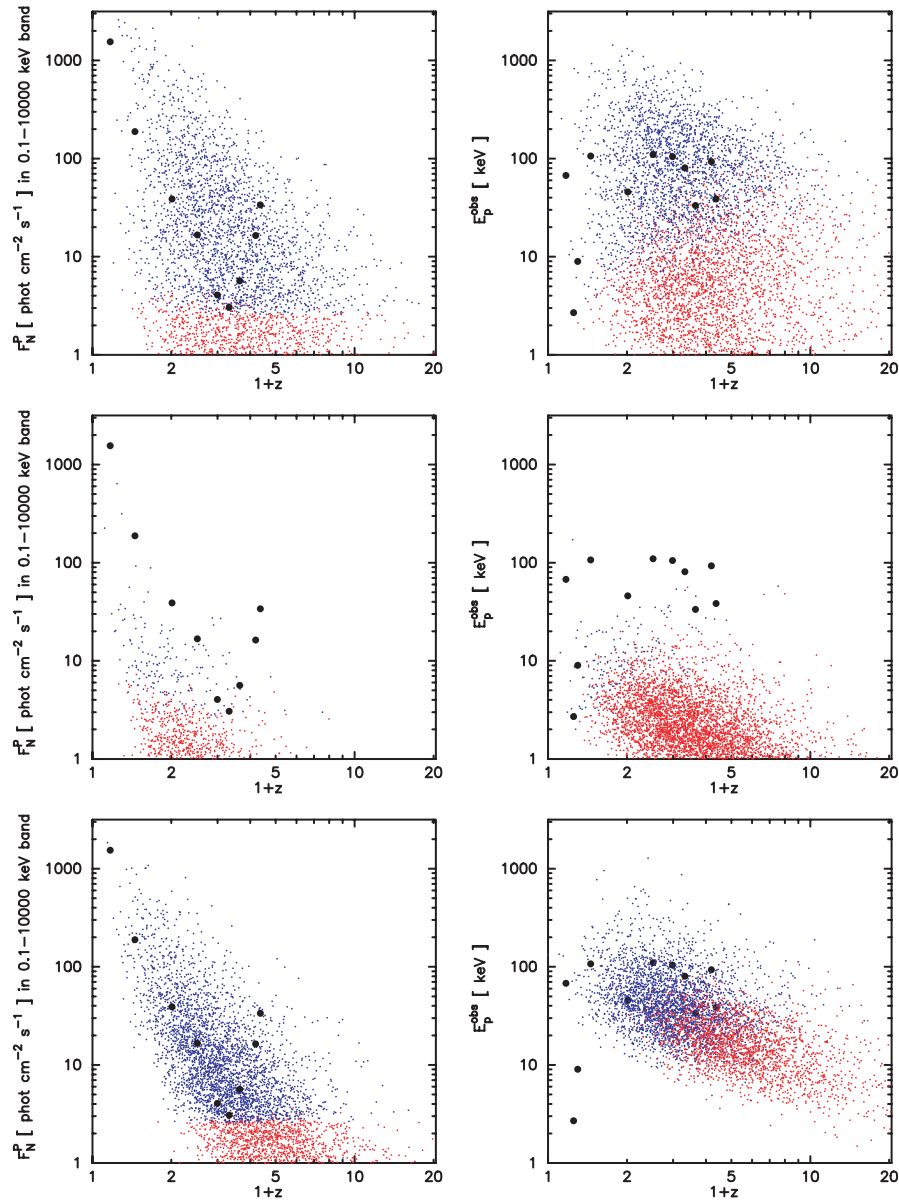
Fig. 15.—Scatter plots of F_N^P (*left*) and E_{peak}^{obs} (*right*) as a function of redshift. The top panels show the distributions of bursts predicted by the variable jet opening angle model for $\delta = 2$. The middle panels show the distributions of bursts predicted by the power-law universal jet model pinned to the E_{iso} value for XRF 020903, while the bottom panels show the distributions of bursts predicted by the power-law universal jet model pinned to the E_{iso} value for GRB 980326. Bursts detected by the WXM are shown in blue and nondetected bursts in red. The filled black circles show the positions of the *BeppoSAX* and *HETE-2* bursts with known redshifts.

S_E and E_{iso}. Taking $N(\Omega_{jet}) \sim \Omega_{jet}^{-2}$ (i.e., $\delta = 2$), the variable jet opening angle model predicts equal numbers of bursts per logarithmic decade in S_E and E_{iso}, which is exactly what *HETE-2* sees (Lamb et al. 2004d; Sakamoto et al. 2004b) (see Figs. 13 and 14). On the other hand, in the power-law universal jet model the probability of viewing the jet at a viewing angle θ_{view}

is $d\Omega_{view}$, where Ω_{view} is the solid angle contained within the angular radius θ_{view}. Consequently, most viewing angles θ_{view} will be $\theta_{view,max}$ or $\approx 90°$, whichever is smaller. This implies that the number of XRFs should exceed the number of GRBs by many orders of magnitude, something that *HETE-2* does not observe (again, see Figs. 13 and 14).

TABLE 2
PERCENTAGES OF XRFs, X-RAY–RICH GRBs, AND HARD GRBs IN *HETE-2* DATA
AND PREDICTED BY DIFFERENT JET MODELS

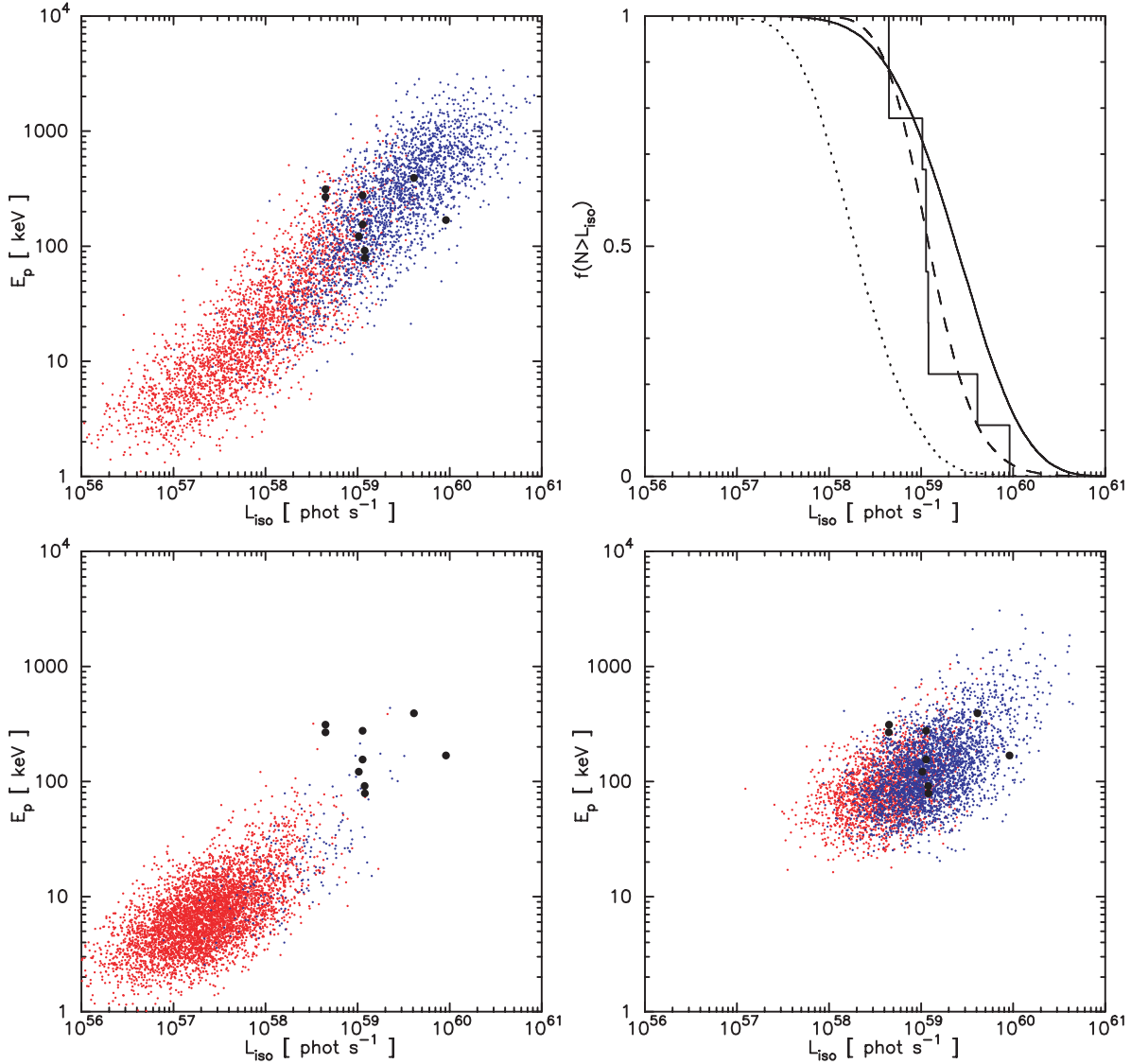| *HETE-2* Data or Model	XRFs (%)	X-Ray–rich GRBs (%)	Hard GRBs (%)
HETE-2 data	33	44	22
Variable opening angle jet	22	39	39
Power-law universal jet pinned to 020903	89	10	1.0
Power-law universal jet pinned to 980326	32	56	12

Fig. 16.—Scatter plots of L_{iso} vs. E_{peak} and comparison of observed and predicted cumulative distributions of L_{iso}. *Top left*: Distribution of bursts predicted by the variable jet opening angle model for $\delta = 2$. Bursts detected by the WXM are shown in blue and nondetected bursts in red. The filled black circles show the positions of the *HETE-2* bursts with known redshifts. *Top right*: Observed cumulative distribution of L_{iso} for *HETE-2* bursts with known redshifts (*histogram*) compared against the cumulative L_{iso} distributions predicted by the variable jet opening angle model for $\delta = 2$ (*solid curve*) and by the power-law universal jet model pinned at the E_{iso} value for XRF 020903 (*dotted curve*) and for GRB 980326 (*dashed curve*). *Bottom left*: Distribution of bursts predicted by the power-law universal jet model pinned at the E_{iso} value for XRF 020903. *Bottom right*: Distribution of bursts predicted by the power-law universal jet model pinned at the E_{iso} value for GRB 980326.

Threshold effects can offset this prediction of the power-law universal jet model over a limited range in S_E and E_{iso}. This is what enables the power-law universal jet model to explain a number of the observed properties of GRBs reasonably well (Rossi et al. 2002; Perna et al. 2003). However, threshold effects cannot offset this prediction over a large range in S_E and E_{iso}, as our simulations confirm. This is why the power-law universal jet model cannot accommodate the large observed ranges in S_E and E_{iso}.

We conclude that if S_E and E_{iso} span ranges of $\sim 10^5$, as the *HETE-2* results strongly suggest, the variable jet opening angle model can provide a unified picture of XRFs and GRBs, whereas the power-law universal jet model cannot. Thus XRFs may provide a powerful probe of GRB jet structure.

6.2. *Rate of GRBs and the Nature of Type Ic Supernovae*

A range in E_{iso} of 10^5, which is what the *HETE-2* results strongly suggest, requires a *minimum* range in $\Delta\Omega_{jet}$ of 10^4–10^5

in the variable jet opening angle model. Thus the unified picture of XRFs and GRBs in the variable jet opening angle model implies that the total number of bursts is

$$N_{total} = -\int_{\Omega_{jet}^{min}}^{\Omega_{jet}^{max}} d\Omega_{jet} \Omega_{jet}^{-2} \approx (\Omega_{jet}^{min})^{-1}. \quad (26)$$

Thus there are $2\pi/\Omega_{jet}^{min} \sim 10^5$ more bursts with very small Ω_{jet} values for every burst that is observable; i.e., the rate of GRBs may be ~ 100 times greater than has been thought.

In addition, since the observed ratio of the rate of Type Ic supernovae (SNe) to the rate of GRBs in the observable universe is $R_{Type Ic}/R_{GRB} \sim 10^5$ (Lamb 1999, 2000), the variable jet opening angle model implies that the rate of GRBs could be comparable to the rate of Type Ic SNe. More spherically symmetric jets yield XRFs, and narrower jets produce GRBs. Thus, low-E_{peak} (intrinsically faint) XRFs may probe core-collapse SNe that produce wide jets, while high-E_{peak} (intrinsically luminous)
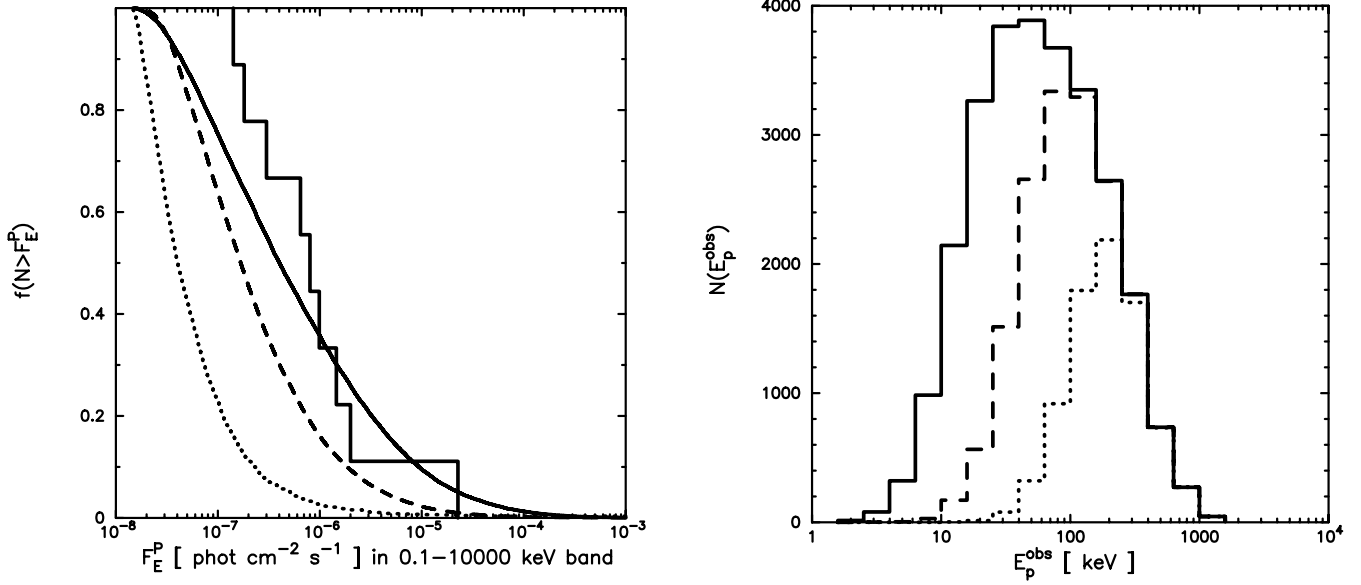
FIG. 17.—*Left*: Comparison of the observed cumulative distribution of F_E^P for *HETE-2* bursts (*histogram*) with the cumulative F_E^P distributions predicted by the variable jet opening angle model for $\delta = 2$ (*solid curve*) and by the power-law universal jet model pinned at the $E_{\rm iso}$ value for XRF 020903 (*dotted curve*) and for GRB 980326 (*dashed curve*). *Right*: Differential distribution of $E_{\rm peak}^{\rm obs}$ predicted by the variable jet opening angle model for $\delta = 2$ for bursts with $F_E^P > 10^{-8}$ (*solid histogram*), 10^{-7} (*dashed histogram*), and 10^{-6} ergs cm^{-2} s^{-1} (*dotted histogram*).

GRBs may probe core-collapse SNe that produce very narrow jets (possibly implying that the cores of the progenitor stars of these bursts are rapidly rotating).

Thus XRFs and GRBs may provide a combination of GRB/SN samples that would enable astronomers to study the relationship between the degree of jetlike behavior of the GRB and the properties of the SN (brightness, polarization ⇔ asphericity of the explosion, velocity of the explosion ⇔ kinetic energy of the explosion, etc.). GRBs may therefore provide a unique laboratory for understanding Type Ic core-collapse SNe.

6.3. *Constraints on $\Omega_{\rm jet}^{\rm min}$ and $\Omega_{\rm jet}^{\rm max}$*

The *HETE-2* results require a range in $\Omega_{\rm jet}$ of $\sim 10^5$ within the context of the variable jet opening angle model in order to explain the observed ranges in S_E and $E_{\rm iso}$. Thus the *HETE-2* results fix the ratio $\Omega_{\rm jet}^{\rm max}/\Omega_{\rm jet}^{\rm min}$, but not $\Omega_{\rm jet}^{\rm min}$ and $\Omega_{\rm jet}^{\rm max}$ separately. However, geometry and observations strongly constrain the possible values of $\Omega_{\rm jet}^{\rm min}$ and $\Omega_{\rm jet}^{\rm max}$. In this paper, we have adopted $\Omega_{\rm jet}^{\rm max} = 0.6 \times 2\pi$ sr (i.e., $\theta_{\rm jet} = 70°$), which is nearly the maximum value allowed by geometry. However, it seems physically unlikely that GRB jets can have jet opening angles as large as $\approx 90°$. One might therefore wish to adopt a smaller value of $\Omega_{\rm jet}^{\rm max}$. This would imply a smaller value of $\Omega_{\rm jet}^{\rm min}$ and therefore a larger GRB rate. But the GRB rate cannot be larger than the rate of Type Ic SNe. Therefore $\Omega_{\rm jet}^{\rm min}$ cannot be much smaller than the value $\Omega_{\rm jet}^{\rm min} = 0.6 \times 2\pi \times 10^{-5}$ sr $= 3.8 \times 10^{-5}$ sr that we have adopted.

Even the value $\Omega_{\rm jet}^{\rm min} = 3 \times 10^{-5}$ sr implies GRB jet opening solid angles that are a factor of ≈ 100 smaller than those inferred from jet break times by Frail et al. (2001), Panaitescu & Kumar (2001), and Bloom et al. (2003). There is a substantial uncertainty in the jet opening solid angle implied by a given jet break time, but the uncertainty is thought to be a factor of ~ 20, not a factor ~ 100 (Rhoads 1999; Sari et al. 1999). In addition, the global modeling of GRB afterglows is largely free from this uncertainty. Such modeling tends to find jet opening angles $\theta_{\rm jet}$ of a few degrees for the brightest and hardest GRBs (Panaitescu & Kumar 2001, 2003)—values of $\theta_{\rm jet}$ that are a factor of at least

3, and in some cases a factor of 10, larger than the jet opening angles we use in this work. This is discomforting; adopting a still smaller value of $\Omega_{\rm jet}^{\rm min}$ would be even more discomforting.

Another constraint on $\Omega_{\rm jet}^{\rm min}$ comes from the monitoring of the late-time radio emission of a sample of 33 nearby Type Ic SNe that has been carried out by Berger et al. (2003c). They find that the energy emitted at radio wavelengths by this sample of Type Ic SNe is $E_{\rm radio} < 10^{48}$ ergs in almost all cases. This implies that these SNe do not produce jets with energies $E_{\rm jet} > 10^{48}$ ergs, and therefore that at most $\sim 4\%$ of all nearby Type Ic SNe produce GRBs, assuming $E_\gamma = 1.4 \times 10^{51}$ ergs. In the variable jet opening angle model, E_γ is a factor of ≈ 100 times less than this value, which weakens the constraint on the allowed fraction of Type Ic SNe that produce GRBs to $\lesssim 10\%$. Adopting a still smaller value of $\Omega_{\rm jet}^{\rm min}$ would decrease E_γ and therefore increase the allowed fraction of Type Ic SNe that produce GRBs. However, a smaller value of $\Omega_{\rm jet}^{\rm min}$ would also increase the predicted numbers (and therefore the fraction) of Type Ic SNe that produce GRBs. Thus, while not yet contradicting the variable jet opening angle model of XRFs and GRBs, the radio monitoring of nearby Type Ic SNe carried out by Berger et al. (2003c) places an important constraint on $\Omega_{\rm jet}^{\rm min}$.

In § 6.6.1 we report tantalizing evidence that the efficiency with which the kinetic energy in the jet is converted into prompt emission at X-ray and γ-ray wavelengths may decrease as $E_{\rm iso}$ and $E_{\rm peak}$ decrease; i.e., this efficiency may be less for XRFs than for GRBs (see also Lloyd-Ronning & Zhang 2004). Since $E_{\rm iso}$ spans 5 decades in going from XRFs to GRBs, even a modest rate of decline in this efficiency with $E_{\rm iso}$ would reduce the required range in $\Delta\Omega_{\rm jet}$ by a factor of 10 or more. Such a factor would allow $\Omega_{\rm jet}^{\rm min}$ to be increased to $\Omega_{\rm jet}^{\rm min} \approx 4 \times 10^{-4}$ sr or more, which would bring the jet opening angle for GRBs in the variable jet opening angle model into approximate agreement with the values derived from global modeling of GRB afterglows. It would also reduce the predicted rate of GRBs by a factor of 10 or more, and therefore also reduce the fraction of Type Ic SNe that produce GRBs to $\sim 10\%$ or less, in agreement with the constraint derived from radio monitoring of nearby

Type Ic SNe. We note that including such a decrease of efficiency with E_{iso} and E_{peak} would introduce an additional parameter into the model.

6.4. *Outliers*

Bloom et al. (2003) and Berger et al. (2003b) have called attention to the fact that not all GRBs have values of E_γ that lie within a factor of 2–3 of the standard energy E_γ, i.e., that there are outliers in the E_γ distribution. Berger et al. (2003c) have also proposed a core-halo model for the jet in GRB 030329.

In addition, we note that the two XRFs for which redshifts or strong redshifts constraints exist (the *HETE*-localized bursts XRF 020903 and XRF 030723) lie squarely on the relation between E_{iso} and E_{peak} found by Amati et al. (2002) (see Fig. 2). The implied value of E_γ from the absence of a jet break in the optical afterglow of XRF 020903 is $\approx 1.1 \times 10^{49}$ ergs (Soderberg et al. 2004), which is consistent with the standard energy of $E_\gamma = 1.17 \times 10^{49}$ ergs that we use in this work. However, the implied value of E_γ from the jet break time of ~ 1 day in XRF 030723 (Dullighan et al. 2003) is a factor of ~ 100 smaller than the standard energy that we use in this work and a factor of $\sim 10^4$ smaller than the standard energy of $E_\gamma = 1.3 \times 10^{51}$ found by Bloom et al. (2003) (see also Frail et al. 2001 and Panaitescu & Kumar 2001).

The unified jet model of XRFs, X-ray–rich GRBs, and GRBs that we have proposed is a phenomenological one and is surely missing important aspects of the GRB jet phenomenon, which may include a significant stochastic element. It therefore cannot be expected to account for the properties of all bursts. Only further observations can say whether the bursts discussed above (or others) are a signal that the unified jet model is missing important aspects of GRB jets, or whether they are truly outliers.

6.5. *Variable Jet Opening Angle Model in the MHD Jet Picture*

Zhang & Mészáros (2002b) and Kumar & Panaitescu (2003) have studied the early afterglows of two GRBs. Zhang & Mészáros (2002b) find in the case of GRB 990123 strong evidence that the jet is magnetic energy dominated; Kumar & Panaitescu (2003) reach a similar conclusion for GRB 021211. In both cases, it appears that the magnetic energy dominated the kinetic energy in the ejected matter by a factor of more than 1000. The recent discovery that the prompt emission from GRB 021206 was strongly polarized (Coburn & Boggs 2003) may provide further support for the picture that GRBs come from magnetic energy–dominated jets.

Part of the motivation for the power-law universal jet model comes from the expectation that in hydrodynamic jets, entrainment and the interaction of the ultrarelativistic outflow with the core of the progenitor star may well result in a strong falloff of the velocity of the flow away from the jet axis. Thus the narrow jets that we find in the unified picture of XRFs, X-ray–rich GRBs, and GRBs based on the variable jet opening angle model are difficult to reconcile with hydrodynamic jets. They may be much easier to understand if GRB jets are magnetic energy dominated, i.e., if GRBs come from MHD jets. Such jets can be quite narrow (Vlahakis & Königl 2001; Proga et al. 2003; Fendt & Ouyed 2004) and may resist the entrainment of material from the core of the progenitor star.

6.6. *Possible Tests of the Variable Jet Opening Angle Model*

6.6.1. *X-Ray and Gamma-Ray Observations*

We have shown that a unified picture of XRFs and GRBs based on the variable jet opening angle model has profound implications for the structure of GRB jets, the rate of GRBs, and
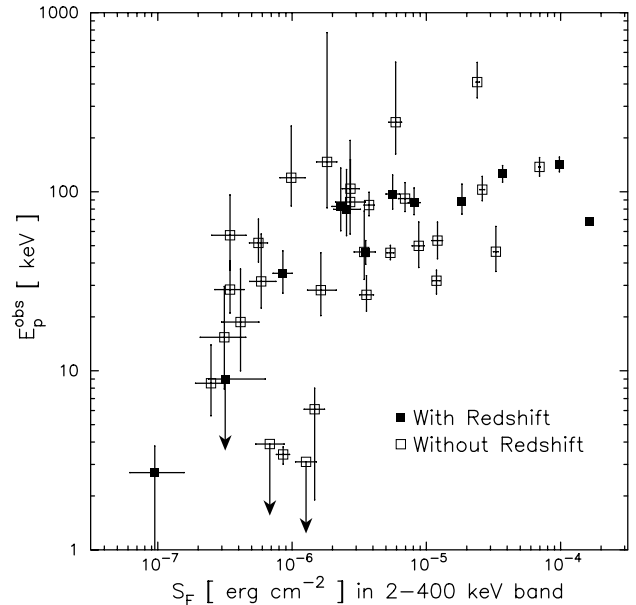

FIG. 18.—Distribution of *HETE*-2 bursts in the $[S(2-400 \text{ keV}), E_{peak}^{obs}]$-plane, showing the bursts with redshift determinations (*filled squares*) and those without (*open squares*). The two events with known redshifts in the lower left-hand corner of the figure are XRF 020903 and XRF 030723. After Sakamoto et al. (2004b).

the nature of Type Ic SNe. Obtaining the evidence needed to confirm (or possibly rule out) the variable jet opening angle model and its implications will require the determination of both the spectral parameters and the redshifts of many more XRFs. The broad energy range of *HETE*-2 (2–400 keV) means that it is able to accurately determine the spectral parameters of the XRFs that it localizes. This will be more difficult for *Swift*, whose spectral coverage (15–150 keV) is more limited.

Until very recently, only one XRF (XRF 020903; Soderberg et al. 2004) had a probable optical afterglow and redshift (see Fig. 18). This is because the X-ray (and by implication the optical) afterglows of XRFs are $\sim 10^3$ times fainter than those of GRBs (see Fig. 19; see also D. Q. Lamb et al. 2005, in preparation). However, we find that the best-fit slope of the correlation between $L_{X,iso}$ and L_{iso} is not $+1$, but $+0.74 \pm 0.17$. This implies that the fraction of the kinetic energy of the jet that goes into the burst itself decreases as L_{iso} (and therefore E_{iso}) decreases; i.e., the fraction of the kinetic energy in the jet that goes into the X-ray and optical afterglow is much larger for XRFs than it is for GRBs.

This result is consistent with a picture in which the central engines of XRFs produce less variability in the outflow of the jet than do the central engines of GRBs, resulting in less efficient extraction of the kinetic energy of the jet in the burst itself in the case of XRFs than in the case of GRBs. Such a picture is supported by studies that suggest that the temporal variability of a burst is a good indicator of the isotropic-equivalent luminosity L_{iso} of the burst (Fenimore & Ramirez-Ruiz 2000; Reichart et al. 2001). These studies imply that XRFs, which are much less luminous than GRBs, should exhibit much less temporal variability than GRBs. As we discussed in § 6.3, if the efficiency with which the kinetic energy in the jet is converted into prompt emission at X-ray and γ-ray wavelengths decreases even modestly with decreasing E_{iso}, it would reduce the required range in $\Delta \Omega_{jet}$ by a factor of 10 or more, allowing the opening angle for GRBs in the variable jet opening angle model to be brought into approximate with the values derived from global modeling of GRB afterglows (Panaitescu & Kumar 2001, 2003) and the rate of GRBs to be brought into agreement with the constraint
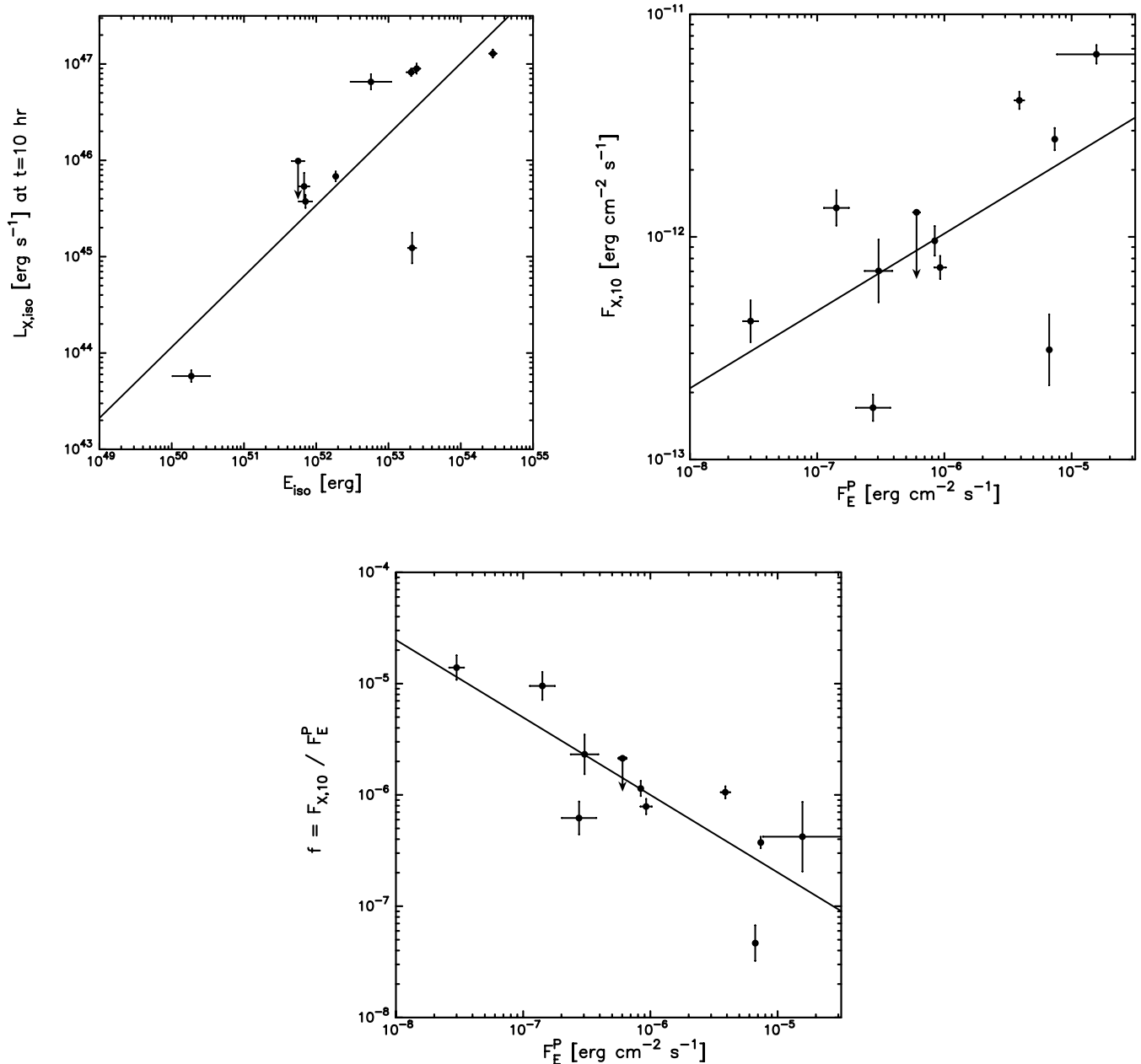
Fig. 19.—*Top left*: Correlation between the isotropic-equivalent burst energy ($E_{\rm iso}$) and the X-ray afterglow luminosity ($L_{\rm X,iso}$) at 10 hr after the burst from Berger et al. (2003a). The slope of the best-fit line is 0.74 ± 0.17 (68% confidence level). *Top right*: Correlation between the X-ray afterglow flux at 10 hr after the burst ($F_{\rm X,10}$) and the peak energy flux (F_E^P). The slope of the best-fit line is 0.35 ± 0.14 (68% confidence level). *Bottom*: The ratio $f = F_{\rm X,10}/F_E^P$ as a function of F_E^P. The slope of the best-fit line is -0.70 ± 0.15 (68% confidence level). After D. Q. Lamb et al. (2005, in preparation).

derived from radio monitoring of nearby Type Ic SNe (Berger et al. 2003c).

The above picture differs from the core-halo picture of GRB jets recently proposed by Berger et al. (2003b), in which the prompt burst emission and the early X-ray and optical afterglows are due to a narrow jet, while the later optical and the radio afterglows are due to a broad jet. In this picture, the total kinetic energy $E_{\rm jet}$ of the jet is roughly constant, but the fraction of $E_{\rm jet}$ that is radiated in the narrow and the broad components can vary.

The challenge presented by the fact that the X-ray (and by implication the optical) afterglows of XRFs are $\sim 10^3$ times fainter than those of GRBs can be met: the recent *HETE-2* localization of XRF 030723 represents the first time that an XRF has been localized in real time (Prigozhin et al. 2003); identification of its X-ray (Butler et al. 2003a, 2003b) and optical

(Fox et al. 2003) afterglows rapidly followed. This suggests that *Swift*'s ability to rapidly follow up GRBs with the XRT and UVOT—its revolutionary feature—will greatly increase the fraction of bursts with known redshifts.

A partnership between *HETE-2* and *Swift*, in which *HETE-2* provides the spectral parameters for XRFs and *Swift* slews to the *HETE-2*–localized XRFs and provides the redshifts, can provide the data that is required in order to confirm (or possibly rule out) the variable jet opening angle model and its implications. This constitutes a compelling scientific case for continuing *HETE-2* during the *Swift* mission.

6.6.2. *Global Modeling of GRB Afterglows*

Panaitescu & Kumar (2003) have modeled in detail the afterglows of GRBs 990510 and 000301c. In both cases, they find

that fits to the X-ray, optical, NIR, and radio data for GRBs 990510 and 000301c favor the variable jet opening angle model over the power-law universal jet model. Detailed modeling of the afterglows of other GRBs may provide further evidence favoring one phenomenological jet model over the other for particular bursts.

6.6.3. *Polarization of GRBs and Their Afterglows*

The variable jet opening angle model and the power-law universal jet model predict different behaviors for the polarization of the optical afterglow. The variable jet opening angle model predicts that the polarization angle should change by $180°$ over time, passing through 0 around the time of the jet break in the afterglow light curve. In contrast, the power-law universal jet model predicts that the polarization angle should not change with time. The polarization data on GRB afterglows that have been obtained to date are in most cases very sparse, making it difficult to tell whether or not the behavior of the polarization favors the variable jet opening angle or the power-law universal jet model.

In the case of GRB 021004, however, the data show clear evidence that the polarization angle changed by approximately $180°$ and changed sign at roughly the time of the jet break, as the variable jet opening angle model, but not the power-law universal jet model, predicts (Rol et al. 2003). Thus, in the case of this one GRB, at least, the behavior of the polarization of the optical afterglow favors the variable jet opening angle model over the power-law universal jet model.

6.7. *Rate of Detection of GRBs by Gravitational Wave Detectors*

If, as the variable jet opening angle model of XRFs, X-ray–rich GRBs, and GRBs implies, most GRBs are bright and have narrow jets, possibly implying that the collapsing core of the progenitor star may be rapidly rotating, then GRBs might be detectable sources of gravitational waves. If, as has been argued, $E_{gw}/E_{rot} \sim 5\%$ in the formation of a black hole from the collapse of the core of a Type Ic SN (van Putten & Levinson 2002), where E_{gw} is the energy emitted in gravitational waves and E_{rot} is the rotational energy of the newly formed black hole, and the rate of GRBs is ~100 times higher than has been thought, then the rate of LIGO/VIRGO detections of GRBs might be ~5 yr^{-1} rather than ~1 yr^{-1} (van Putten & Levinson 2002).

7. CONCLUSIONS

In this paper we have shown that a variable jet opening angle model, in which the isotropic-equivalent energy E_{iso} depends on the jet solid opening angle Ω_{jet}, can account for many of the observed properties of XRFs, X-ray–rich GRBs, and GRBs in a unified way. We have also shown that although the power-law universal jet model can account reasonably well for many of the observed properties of GRBs, it cannot easily be extended to accommodate XRFs and X-ray–rich GRBs. The variable jet opening angle model implies that the total radiated energy in gamma rays E_{γ} is ~100 times smaller than has been thought. The model also implies that the hardest and most brilliant GRBs have jet solid angles $\Omega_{jet}/2\pi \sim 10^{-5}$. Such small solid angles are difficult to achieve with hydrodynamic jets and lend support to the idea that GRB jets are magnetic energy dominated. Finally, the variable jet opening angle model implies that there are $\sim10^5$ more bursts with very small Ω_{jet} values for every observable burst. The observed ratio of the rate of Type Ic SNe to the rate of GRBs is $R_{Type\,Ic}/R_{GRB} \sim 10^5$; the variable jet opening angle model therefore implies that the GRB rate may be comparable to the rate of Type Ic SNe, with more spherically symmetric jets yielding XRFs and narrower jets producing GRBs. GRBs may therefore provide a unique laboratory for understanding Type Ic core-collapse SNe.

REFERENCES

Amati, L., et al. 2002, A&A, 390, 81
Atteia, J.-L., et al. 2003, in AIP Conf. Proc. 662, Gamma-Ray Burst and Afterglow Astronomy 2001, ed. G. R. Ricker & R. K. Vanderspek (New York: AIP), 17
Band, D. L. 2003, ApJ, 588, 945
Band, D. L., et al. 1993, ApJ, 413, 281
Barraud, C., et al. 2003, A&A, 400, 1021
Berger, E., Kulkarni, S. R., Frail, D. A., & Soderberg, A. M. 2003a, ApJ, 590, 379
Berger, E., et al. 2003b, Nature, 426, 154
———. 2003c, ApJ, 599, 408
Bloom, J., Frail, D. A., & Kulkarni, S. R. 2003, ApJ, 588, 945
Butler, N., et al. 2003a, GCN Circ. 2328, http://gcn.gsfc.nasa.gov/gcn/gcn3/2328.gcn3
———. 2003b, GCN Circ. 2347, http://gcn.gsfc.nasa.gov/gcn/gcn3/2347.gcn3
Coburn, W., & Boggs, S. E. 2003, Nature, 423, 415
Dermer, C. D., Chiang, J., & Böttcher, M. 1999, ApJ, 513, 656
Dermer, C. D., & Mitman, K. E. 2004, in ASP Conf. Ser. 312, Third Rome Workshop on Gamma-Ray Bursts in the Afterglow Era, ed. M. Feroci, F. Frontera, N. Masetti, & L. Piro (San Francisco: ASP), 301
Donaghy, T. Q., Lamb, D. Q., & Graziani, C. 2004a, ApJ, submitted
———. 2004b, in AIP Conf. Proc. 727, Gamma-Ray Bursts: 30 Years of Discovery, ed. E. E. Fenimore & M. Galassi (Melville: AIP), 47
Dullighan, A., Butler, N., Vanderspek, E., Villasenor, J., & Ricker, G. 2003, GCN Circ. 2336, http://gcn.gsfc.nasa.gov/gcn/gcn3/2336.gcn3
Fendt, C., & Ouyed, R. 2004, ApJ, 608, 378
Fenimore, E. E., & Ramirez-Ruiz, E. 2000, preprint (astro-ph/0004176)
Fox, D. W., et al. 2003, GCN Circ. 2323, http://gcn.gsfc.nasa.gov/gcn/gcn3/2323.gcn3
Frail, D., et al. 2001, ApJ, 562, L55
Heise, J., in 't Zand, J., Kippen, R. M., & Woods, P. M. 2000, in Proc. 2nd Rome Workshop: Gamma-Ray Bursts in the Afterglow Era, ed. E. Costa, F. Frontera, & J. Hjorth (Berlin: Springer), 16
Huang, Y. F., Dai, Z. G., & Lu, T. 2002, MNRAS, 332, 735
Kawai, N., et al. 2003, in AIP Conf. Proc. 662, Gamma-Ray Burst and Afterglow Astronomy 2001, ed. G. R. Ricker & R. K. Vanderspek (New York: AIP), 25
Kippen, R. M., Woods, P. M., Heise, J., in 't Zand, J., Briggs, M. S., & Preece, R. D. 2003, in AIP Conf. Proc. 662, Gamma-Ray Burst and Afterglow Astronomy 2001, ed. G. R. Ricker & R. K. Vanderspek (New York: AIP), 244
Kumar, P., & Panaitescu, A. 2003, MNRAS, 346, 905
Lamb, D. Q. 1999, A&AS, 138, 607
———. 2000, Phys. Rep., 333, 505
Lamb, D. Q., Donaghy, T. Q., & Graziani, C. 2004a, NewA Rev., 48, 423
———. 2004b, in Cosmic Explosions in Three Dimensions, ed. P. Höflich, P. Kumar, & J. C. Wheeler (Cambridge: Cambridge Univ. Press), 327
———. 2004c, in AIP Conf. Proc. 727, Gamma-Ray Bursts: 30 Years of Discovery, ed. E. E. Fenimore & M. Galassi (Melville: AIP), 19
Lamb, D. Q., et al. 2004d, ApJ, submitted
Liang, E. W., Dai, Z. G., & Wu, X. F. 2004, ApJ, 606, L29
Lloyd-Ronning, N., Fryer, C., & Ramirez-Ruiz, E. 2002, ApJ, 574, 554
Lloyd-Ronning, N., Petrosian, V., & Mallozzi, R. S. 2000, ApJ, 534, 227
Lloyd-Ronning, N., & Zhang, B. 2004, ApJ, 613, 477

Mészáros, P., Ramirez-Ruiz, E., Rees, M. J., & Zhang, B. 2002, ApJ, 578, 812
Mochkovitch, R., Daigne, F., Barraud, C., & Atteia, J. L. 2004, in ASP Conf. Ser. 312, Third Rome Workshop on Gamma-Ray Bursts in the Afterglow Era, ed. M. Feroci, F. Frontera, N. Masetti, & L. Piro (San Francisco: ASP), 381
Panaitescu, A., & Kumar, P. 2001, ApJ, 560, L49
———. 2003, ApJ, 592, 390
Perna, R., Sari, R., & Frail, D. 2003, ApJ, 594, 379
Preece, R., et al. 2000, ApJS, 126, 19
Prigozhin, G., et al. 2003, GCN Circ. 2313, http://gcn.gsfc.nasa.gov/gcn/gcn3/2313.gcn3
Proga, D., MacFadyen, A. I., Armitage, P. J., & Begelman, M. C. 2003, ApJ, 599, L5
Ramirez-Ruiz, E., & Lloyd-Ronning, N. 2002, NewA, 7, 197
Reichart, D. E., & Lamb, D. Q. 2001, in AIP Conf. Proc. 586, 20th Texas Symposium on Relativistic Astrophysics, ed. J. C. Wheeler & H. Martel (New York: AIP), 599
Reichart, D. E., et al. 2001, ApJ, 552, 57
Rhoads, J. E. 1999, ApJ, 525, 737
Ricker, G. R., et al. 2003, in AIP Conf. Proc. 662, Gamma-Ray Burst and Afterglow Astronomy 2001, ed. G. R. Ricker & R. K. Vanderspek (New York: AIP), 3

Rol, E., et al. 2003, A&A, 405, L23
Rossi, E., Lazzati, D., & Rees, M. J. 2002, MNRAS, 332, 945
Rowan-Robinson, M. 2001, ApJ, 549, 745
Sakamoto, T., et al. 2004a, ApJ, 602, 875
———. 2004b, ApJ, submitted
Sari, R., Piran, T., & Halpern, J. P. 1999, ApJ, 519, L17
Schmidt, M. 2001, ApJ, 552, 36
Soderberg, A. M., et al. 2004, ApJ, 606, 994
van Putten, M. H. P. M., & Levinson, A. 2002, Classical Quantum Gravity, 19, 1309
Vlahakis, N., & Königl, A. 2001, ApJ, 563, L129
Yamazaki, R., Ioka, K., & Nakamura, T. 2002, ApJ, 571, L31
———. 2003, ApJ, 593, 941
Yonetoku, D., Murakami, T., Nakamura, T., Yamazaki, R., Inoue, A. K., & Ioka, K. 2004, ApJ, 609, 935
Zhang, B., Dai, X., Lloyd-Ronning, N. M., & Mészáros, P. 2004a, ApJ, 601, L119
Zhang, B., & Mészáros, P. 2002a, ApJ, 571, 876
———. 2002b, ApJ, 581, 1236
Zhang, W., Woosley, S. E., & Heger, A. 2004b, ApJ, 608, 365